THE JOURNAL OF PHYSICAL CHEMISTRY C

pubs.acs.org/JPCC

Article

Adsorption of NO_2 and NO_3 on Cobalt Spinel Nanocubes and Interfacial Dynamics of the Resultant NO_x Adspecies (x = 1, 2, and 3): DFT, Atomistic Thermodynamic, IR, and Isotopic Exchange Study

Filip Zasada,* Pâmella Vasconcelos Borges Pinho, Witold Piskorz, Camillo Hudy, Janusz Janas, Joanna Gryboś, Kinga Góra-Marek, and Zbigniew Sojka

Cite This: *J. Phys. Chem. C* 2020, 124, 19681−19697

Read Online

ACCESS | Metrics & More | Article Recommendations | Supporting Information

ABSTRACT: Periodic GGA+U and atomistic thermodynamic modeling, combined with IR and isotopic exchange investigations, were employed for comprehensive description of NO_2 and NO_3 adsorption on the (100) surface of Co_3O_4 nanocubes. A wide range of identified NO_2 and NO_3 adspecies includes N- and O-bound monodentate (η^1), bidentate (η^2), bridging bidentate (μ-η^2), and bridging monodentate (μ-η^1:η^1) surface complexes. The most stable were the bridging μ-η^1(O):η^1(O)-Co^T−ONO−Co^O (−1.91 eV) and chelating η^2(O,O)-NO_2−Co^T (E_{ads} = −1.87 eV) adducts over dual tetrahedral (Co^T_{2c}) and ocatehedral (Co^O_{5c}) sites, whereas the μ-η^1(O):η^1(O)-Co^O−ONO−Co^O (−1.25 eV) and η^2(O,O)-NO_2−Co^O (−1.57 eV) adducts of the Co^O centers only were less strongly bound. The DOS structure, spin density repartition, and atomic partial charge analysis were used for detailed interpretation of the electronic structure of the most stable NO_2 and NO_3 adducts. Thermodynamic $\Theta_{NO_2} = f(p_{NO_2}, T)$ diagrams were constructed for quantitative interpretation of the NO_2 and NO_3 adsorption on the (100) surface. A complex set of intermolecular surface O ↔NO ↔ NO_2↔ NO_3 dynamics was thoroughly examined and applied for elucidation of an intricate mechanism of the NO_2 and NO_3 desorption, NO oxidation, and $N^{16}O/N^{18}O$ isotopic exchange, providing a scientific background for SCR, deNOx, or NO_x-sensing reactions as well.

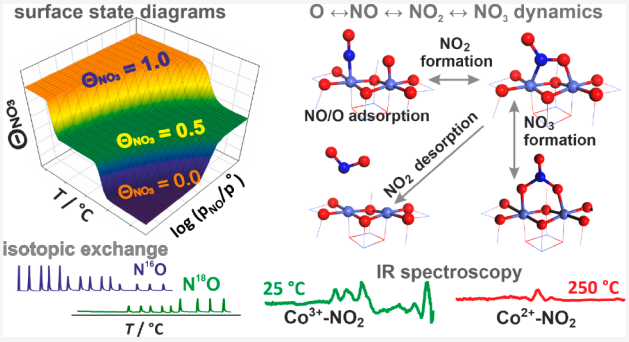

1. INTRODUCTION

Noxious exhaust gases emitted from stationary sources and combustion vehicles contain various nitrogen oxides that contribute to the smog development, acid rains, ozone depletion, and the greenhouse effect as well.[1] Efficient abatement of such contaminants below the permitted emission levels is one of the prime challenges for environmental catalysis, and for this purpose various catalytic processes have been developed so far.[2] Apart from the most common NO and NO_2 nitrogen oxides, there is an increasing concern about lesser known NO_3 species.[3,4] Nitrogen trioxide produced by the reaction of NO_2 with ozone has been recognized as a critical intermediate influencing the pollution chemistry of the nocturnal atmosphere. Acting as an efficient abstractor of the hydrogen atom from VOC molecules, it is also involved in the production of atmospheric nitric acid.[5] On oxide catalytic surfaces, NO_3 and NO_2 (often in the form of the congener NO_3^- and NO_2^- anions) may be produced via NO_2 disproportionation or NO/NO_2 oxidation.[6]

The two prime processes for NO_x elimination include direct decomposition into elements (deNOx)[7−9] and selective catalytic reduction (SCR) by using various hydrocarbons[10−12] or NH_3.[13−16] Both reactions can be promoted significantly by oxidation of NO into NO_2 (fast SCR).[17] The catalytic oxidation of NO to NO_2 is then a key step for effective NO_x removal in various SCR processes,[18] including the NO_x storage−reduction (NSR) variants.[19] In this context, it is worth mentioning that NO_x gases are also foremd in an undesired side reaction of the nonselective ammonia oxidation that competes with the main SCR process.[20−22]

Numerous studies on developing robust catalysts for NO oxidation exploring different types of heterogeneous catalysts have been reported[23−26] Supported systems containing platinum group metals have been identified as one of the most active.[27,26,28] However, transition oxide spinel catalysts have been found to exhibit competing activities for NO oxidation.[29,30] It is also worth mentioning that rapid oxidation

Received: July 7, 2020
Revised: July 26, 2020
Published: July 27, 2020

https://dx.doi.org/10.1021/acs.jpcc.0c06195
J. Phys. Chem. C 2020, 124, 19681−19697

of nitric oxide is particularly beneficial for diesel soot abetment,[8,31] and recently reported mixed mesoporous $M_xCo_{3-x}O_4$ spinels (M = Zn and Ni) show impressive catalytic activity in NO_x-mediated soot combustion.[32] Nitric oxides are also involved in N_2O elimination from tail gases of nitric acid plants as a most harmful contaminant for low-temperature oxide catalysts. Various surface and bulk-promoted cobalt spinel catalysts belong to the most active materials for this process.[33−36] The presence of nitric oxide in the feed, however, substantially deteriorates the catalytic performance of Co_3O_4, due to formation of various NO_x adspecies that are blocking active sites.[37] Indeed, in the presence of NO in the feed, the reactive surface oxygen intermediates present on the cobalt spinel surface may interact with the gas phase and/or adsorbed NO molecules, giving rise to the formation of various NO_x adspecies that are strongly attached to the surface. Nature, electronic structure, and surface dynamics of those species are not comprehensively elucidated as yet. Co_3O_4 is also a good catalyst for NO oxidation, even at low temperatures and high space velocities, and the catalysts calcined at 300 °C show the maximum yield of nitrogen dioxide formation.[38,39]

The high sensitivity of cobalt spinel to NO and NO_2 capture has been used for the development of the p-type Co_3O_4[40,41] and mixed cobalt spinel sensor devices[42] for the detection of nitric oxides. It is presumed that NO_2 molecules reacting with the chemisorbed oxygen species lead to the formation of NO_3^- adspecies, which is directly reflected in changes of the sensor resistance. To explore sensing capabilities of the Co_3O_4 nanostructures, the chemical state of the NO_2 and NO adspecies and their surface dynamics in the presence of oxygen at the temperature of the sensor operation has to be thoroughly elucidated. It provides for a suitable molecular background for understanding the detection mechanism in the requisite detail.

Catalytic performance of the nanocrystalline cobalt spinel catalysts is highly influenced by the structure of the exposed planes and the presence of defects such as oxygen vacancies in particular.[43−47] Survey of the experimental data shows that the Co_3O_4 catalysts prepared by conventional methods are mainly faceted on the (100) and (111) planes with a small and scarce share of the (110) termination only.[48−50] Furthermore, a quite straightforward hydrothermal synthesis Co_3O_4 nanocrystals of the cubic shape allows for their widespread application as a versatile model system for rigorous investigations into the structure−catalytic activity relationship of this redox intricate benchmarking catalytic system.

Thorough molecular-level studies of the interaction of nitrogen di- and trioxides with cobalt spinel surface are scarcely addressed in the literature, so we performed systematic DFT investigations combined with *ab initio* thermodynamic modeling into the adsorption and surface dynamics of NO_2 and NO_3 on the (100) surface exposed by cobalt spinel nanocubes. The computational studies were corroborated by IR and isotopic exchange measurements.

2. COMPUTATIONAL AND EXPERIMENTAL DETAILS

2.1. DFT Calculations. For the performed periodic VASP calculations, a spin unrestricted DFT+*U* level of theory with PAW scheme and GGA-PW91[51] exchange-functional were employed. The Hubbard *U* parameter was set to *U* = 3.0 eV for the Co ions, following the previous literature.[52,53] The Monkhorst−Pack mesh[54] of the 5 × 5 × 5 density for bulk and 5 × 5 × 1 for slab calculations with the cutoff energy of 500 eV were used for the Brillouin zone sampling. The Methfessel−Paxton[55] smearing parameter set to σ = 0.1 eV, and the SCF equations were solved with the convergence limit set to 10^{-5} eV. The bulk cobalt spinel unit cell was obtained by optimizing the experimental cubic (1 × 1 × 1) cell containing 56 ions (within an error of 10^{-3} eV/Å), upon fitting the calculated *E*/*V* values to the Birch−Murnaghan equation.[56] The surface (1 × 1) slab models of the $Co_{30}O_{40}$ stoichiometry were constructed by cutting the optimized bulk structure in the [100] direction. The thickness of the oxide layer is ∼10 Å (11 atomic sheets), and the vacuum separation between them was equal to ∼12 Å. An apposite symmetry of the top and bottom terminations was ascertained to minimize development of the dipole moment within the supercells. Full relaxation of the atomic positions was allowed only for the three top and three bottom layers, since the changes in the atomic positions in deeper sublayers were insignificant (for details, see Figure S1). The atomic charges were calculated employing the Bader scheme,[57] whereas the local magnetic moments were derived from the difference of the spin up and down charges in the Wigner spheres, centered at the atomic positions. Transition states (TS) were calculated within the nudged elastic band approach (NEB),[58] and 5−9 NEB images were used for this aim.

2.2. First-Principles Thermodynamics. The free enthalpy of NO_x (*x* = 1, 2, and 3) adsorption, $\Delta_a G^{tot}_{surf}$, were expressed as a difference between the corresponding values of the slab model covered by n_i NO_x molecules ($G^{slab}(T, p_i, n_i)$), and the sum of the free enthalpies of the bare surface ($G^{slab}(T, p)$) and the gaseous NO_x species ($G^{gas}_i(T, p_i)$):[59]

$$\Delta_a G^{tot.}_{surf.}(T, p_i, n_i) = G^{slab}(T, p_i, n_i) - [G^{slab}(T, p) + G^{gas}_i(T, p_i)] \quad (1)$$

The free enthalpy of the slab was next approximated as $\Delta G^{slab} \approx \Delta E^{slab}$, while the $\Delta_a G^{tot}_{surf}$ term (eq 2) was factorized into an electronic contribution ($\Delta_a E^{el}$), calculated as the difference of the DFT energies (eq 3) and the change in the chemical potential of the NO_x molecules upon adsorption of n_i species on the surface ($n_i\Delta\mu_i$, see eq 4).

$$\Delta_a G^{tot.}_{surf.}(T, p_i, n_i) = \Delta_a E^{el} - n_i\Delta\mu_i \quad (2)$$

$$\Delta_a E^{el} = E^{el}((100)/n\mathrm{NO}_x) - E^{el}((100)) - nE^{el}(n\mathrm{NO}_x) \quad (3)$$

$$\Delta\mu_i(T, p_i) = \Delta\mu^\circ(T) + RT\ln(p_i/p^\circ) \quad (4)$$

The standard $\Delta\mu^\circ(T)$ potential was calculated by means of the statistical thermodynamics, whereas for the temperature and pressure dependence of the surface coverage, $\Theta(p,T)$ a multisite Langmuir isotherm model was applied[60,61] (for details, see the Supporting Information section S2).

2.3. Experimental Methods. Cobalt spinel nanocrystals of cubic shape were synthesized by the hydrothermal method (180 °C, 3 h), using a Teflon-lined steel autoclave, and a precursor mixture of 0.01 mol of $Co(NO_3)_2{\cdot}6H_2O$ and 0.005 mol of NaOH (Merk) dissolved in 10 mL of water. The obtained spinel catalyst was washed several times with distilled water and then dried at 60 °C for 12 h. The relevant physicochemical characterization of the Co_3O_4 sample, confirming high quality and an euhedral shape of the

https://dx.doi.org/10.1021/acs.jpcc.0c06195
J. Phys. Chem. C 2020, 124, 19681−19697

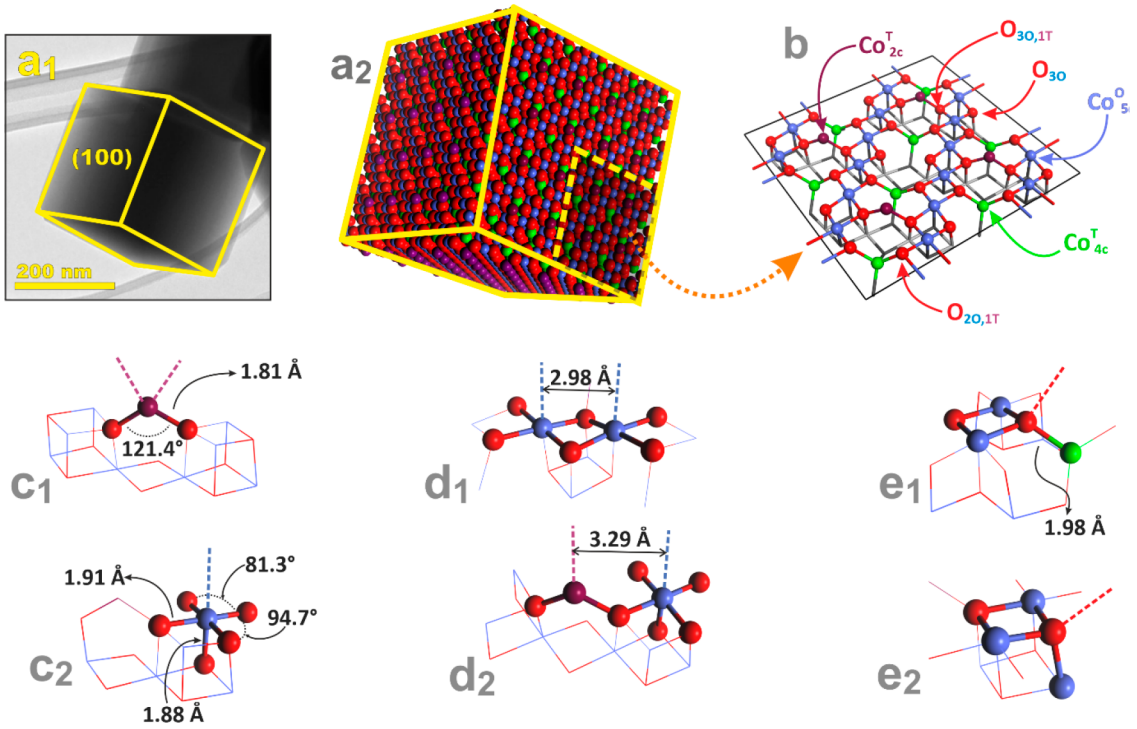

Figure 1. TEM picture of a cobalt spinel cubic nanocrystal (a_1) together with the corresponding CPK model (a_2). The ball and stick perspective view of the (2 × 2) element of the (100) surface, defining the surface sites and their labeling (b). The geometric structure of single cationic (c_1,c_2), double cationic (d_1,d_2), and anionic (e_1,e_2) adsorption sites on the cobalt spinel (100) facet. Color coding: surface Co^{T}_{2c} (purple); subsurface Co^{T}_{4c} (green); Co^{O}_{5c} (blue); and O (red).

synthesized nanocrystals is reported in the Supporting Information section S3.

Surface sate of the adsorbed NO_x species was examined by FT-IR spectroscopy with the 2 cm^{-1} spectral resolution, using a Vertex 70 spectrometer with the MCT detector. Before the measurements, the self-supporting wafers (40 mg of the Co_3O_4 catalyst diluted with 10 mg of SiO_2) were pretreated *in situ* at 450 °C *in vacuo* for 1 h and then in 1% O_2 at 300 °C for 1 h. Nitrogen monoxide was adsorbed at room temperature, under the pressure of 5−10 Torr, and the physisorbed and the remaining gas phase NO were removed by evacuation. For evaluation of the thermal stability of the chemisorbed NO_x species, the evacuation temperature was increased up to 400 °C. The thermo-programmed isotopic exchange experiments were performed in the range of 25−600 °C, by pulsing $N^{16}O$ on the cobalt spinel surface covered by the ^{18}O-labeled oxygen adspecies. The gas composition measurements were carried out by means of a QMS detector (Hiden Analytical HPR20), and a quartz flow reactor with 200 mg of the catalyst (sieve fraction of 0.2−0.3 mm), under the flow of 30 mL·min^{-1} and the heating rate of 10 °C·min^{-1} was used in those experiments.

3. RESULTS

3.1. Bulk and Surface Characteristics of Co_3O_4 Nanocubes. For validation of the spinel structure modeling, we briefly compared the calculated geometric, electronic, and magnetic parameters with the available experimental values, and collation of the results is presented in the Supporting Information section S4. A good agreement between the calculated and experimental data reveals that the applied atomistic model and the calculation scheme were adequate for accurate modeling of the cobalt spinel structure and surface energetics.

The TEM image of a cobalt spinel nanograin (Figure 1a_1) reveals its euhedral cubic shape, whereas the corresponding space-filling model (CPK) (Figure 1a_2) shows the overall arrangement of the constituent atoms on the exposed (100) plane. A more detailed picture presenting the 2 × 2 (100) surface element (Figure 1b) shows that this termination is composed of truncated octahedral Co^{O}_{5c} ions (coded blue; the subscript indicates their actual coordination number), exposed truncated tetrahedral Co^{T}_{2c} ions (purple), and dipped tetrahedral Co^{T}_{4c} ions of regular coordination (green). The anionic sublattice is constituted by 3-fold coordinated oxygen ions (O_{3O}) bound to Co^{O} exclusively, four 3-fold coordinated anions ($O_{2O,1T}$) linked to two Co^{O} and to a Co^{T} cation, and two fully coordinated $O_{3O,1T}$ species (all O atoms are shown in red). The structure of the single cationic sites is presented in Figure 1c_1,c_2, where the dangling bonds are marked by dashed lines. Dual cationic sites on the (100) surface can also be involved in the NO_x adsorption due to the small intercationic distances ($d_{Co\cdots Co}$). For the dual $Co^{O}\cdots Co^{O}$ sites (Figure 1d_1), such a distance $d_{Co\cdots Co}$ is 2.98 Å, whereas in the case of $Co^{T}\cdots Co^{O}$ pairs (Figure 1d_2), it is longer (3.29 Å). The bridging geometries of the NO_x binding are therefore achievable on those both kinds of the adsorption sites (see below). For the sake of completeness, we also took into account the single anionic $O_{2O,1T}$ and O_{3O} centers (Figures 1e_1,e_2) while modeling the NO_x adsorption modes.

The electronic and magnetic structure of the ions exposed on the (100) termination are shown in Figure S3. For all surface ions, the Bader charge analysis showed only small changes in comparison to bulk values. Inspection of the spin density repartition revealed an open-shell nature of all the surface cations (see Figure S3b). The magnetic moments (Figure S3c) were preserved for the Co^{T}_{2c} ions ($\mu \cong 2.6\ \mu_B$, S

https://dx.doi.org/10.1021/acs.jpcc.0c06195
J. Phys. Chem. C 2020, 124, 19681−19697

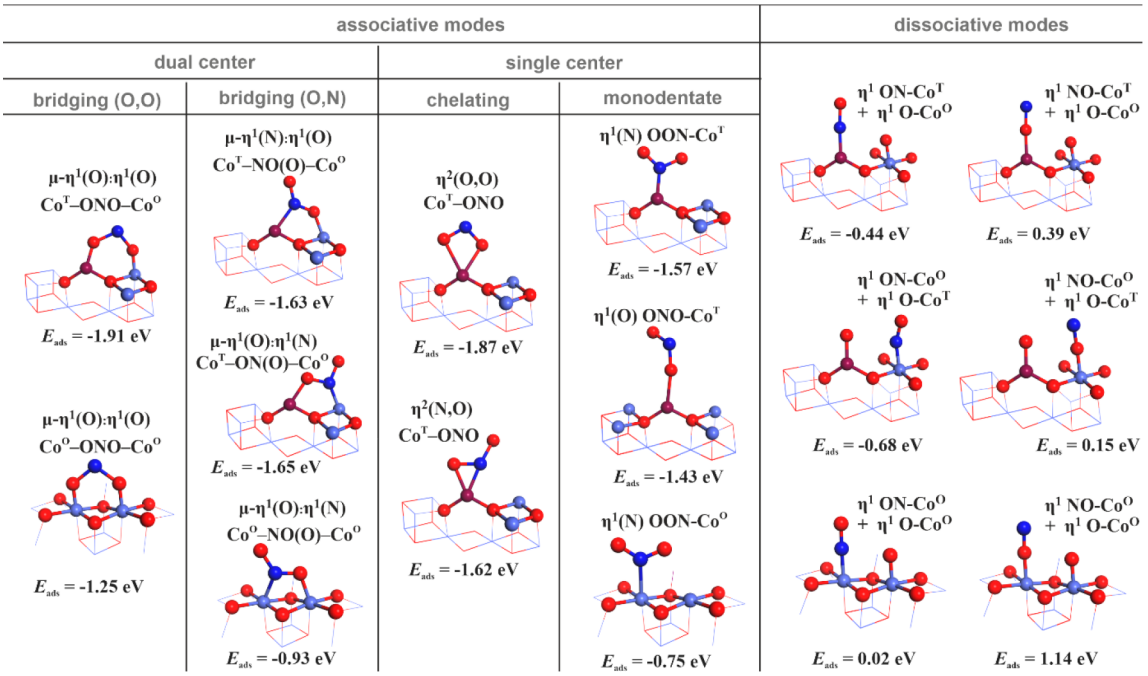

Figure 2. Conceivable associative and dissociative modes of NO_2 adsorption on the (100) Co_3O_4 surface together with the corresponding adsorption energies (E_{ads}). Color coding: $Co^T{}_{2c}$, purple; $Co^O{}_{5c}$, light blue; N, dark blue; and O, red.

= 3/2), whereas low (~0 μ_B, S = 0) to high spin (~1.9 μ_B, S = 1) transition takes place in the case of the surface $Co^O{}_{5c}$ centers.[63] The calculated charges and magnetization values of both cobalt sites were used as the convenient reference points, while examining changes in their oxidation states induced by the adsorption of NO, NO_2, and NO_3 molecules on the (100) surface of Co_3O_4.

3.2. NO_2 Adsorption. Taking into account that nitrogen monoxide is not only a product of dissociative adsorption of NO_2 and NO_3 but also a precursor molecule for their on-surface formation upon NO adsorption in the presence of oxygen, we briefly recalled in the Supporting Information section S6, the most important modes of the NO attachment, which are implicated in the complex NO−NO_2−NO_3 surface dynamics. A thorough study of all possible surface NO adducts, including a detailed analysis of their electronic and magnetic structures, has been described in our previous paper.[62] Interaction of NO_2 molecules with the (100) surface gives rise a large variety of conceivable topological and conformational configurations (Figure 2).

Associative adsorption modes include bridging (μ-η^1;η^1) attachment of NO_2 to the dual [Co^T···Co^O] or [Co^O···Co^O] centers (Figure 2, the first and second column), occurring through the two terminal oxygen (O,O) or oxygen and nitrogen atoms (O,N), together with the bidentate (η^2) and monodentate (η^1) binding isomers involving single cobalt centers only (Figure 2, the third and fourth column, respectively). Dissociative modes lead to coexistence of the NO and O fragments adsorbed on the [Co^T···Co^O] and [Co^O···Co^O] cationic pairs. Since NO ligand can be attached through oxygen or nitrogen moiety, there are six different possible conformations shown in the right column of Figure 2.

A brief inspection of the NO_2 adsorption energetics (Figure 2) reveals that only associative forms exhibit significant adsorption energies. Among them, the O-down surface adducts are the most stable with E_{ads} = −1.91 and −1.87 eV for the bridging μ-η^1(O):η^1(O)-Co^T−ONO−Co^O and the chelating η^2(O,O)-NO_2−Co^T species, respectively. The bridging μ-η^1(N):η^1(O) modes of NO_2 adsorption on the [Co^T···Co^O] pairs (Co^T−N(O)O−Co^O and Co^T−O(O)N−Co^O adducts), together with single-center bidentate, η^2(O,N) and monodentate η^1(N) and η^1(O) conformations of the NO_2 attachment to the Co^T centers, are characterized by similar adsorption energies (E_{ads} = −1.63, −1.65, −1.62,−1.57, and −1.43 eV, respectively). This fact, along with an apparent geometrical resemblance (all adspecies are connected to the Co^T sites), allows for the coexistence of such adducts on the (100) surface, and their mutual transformation one into another. The adducts stabilized exclusively on the Co^O sites, such as the bridging μ-η^1(O):η^1(O)-Co^O−ONO−Co^O and μ-η^1(N):η^1(O)-Co^O−ONO−Co^O adspecies, as well as the monodentate η^1(N)-OON−Co^O adducts, are characterized by lower adsorption energies (E_{ads} = −1.25, −0.93, and −0.75 eV, respectively). The adsorption energies of the dissociative forms (calculated versus gas-phase NO_2) point to their lower stability in comparison with the associative counterparts (Figure 2). Moreover, only the configurations comprising the adducts stabilized through nitrogen atom are thermodynamically stable. The ON−O bond cleavage upon adsorption of NO_2 is rather energetically demanding, especially for the bridged forms attached through the O atoms (see below, Figure 10). The unfavorable dissociation energetics implies that the NO molecules accommodated on the (100) surface covered with monatomic oxygen intermediates can readily be oxidized into NO_2 adspecies ($NO_{(ads)} + O_{(ads)} \rightarrow NO_{2(ads)}$). For this reaction the energetically most advantageous starting species are the {η^1-ON−Co^T, η^1-O−Co^T} and {η^1-O−Co^T, η^1-ON−Co^O} pairs, where NO is ligated through nitrogen atom on the $Co^T{}_{2c}$ or $Co^O{}_{5c}$ centers, respectively. Such configurations may readily (in a one-step bond-formation process) produce the bridging μ-η^1(N):η^1(O)-Co^T−N(O)O−Co^O and

https://dx.doi.org/10.1021/acs.jpcc.0c06195
J. Phys. Chem. C 2020, 124, 19681−19697

Table 1. Energetics, Geometry, Partial Charge (q_B), and Magnetization (μ) of the Most Stable Associative Modes of NO_2 Adsorption on the (100) Termination of Cobalt Spinel, together with the Corresponding Reference Values Calculated for the Bare (100) Surface and Gas-Phase $NO_{2(g)}$

	adsorption modes					reference states	
properties	μ-η^1:η^1-Co^T–ONO–Co^O	μ-η^1:η^1-Co^O–ONO–Co^O	η^2-NO_2–Co^T	η^1-O_2N–Co^T	η^1-ONO–Co^T	(100)-S	NO_2
E_{ads}/eV	−1.91	−1.24	−1.94	−1.57	−1.43		
d_{Co-NO_2}/Å	1.92; 2.07	1.96/1.97	2.03	1.92	1.87		
d_{N-O}/Å	1.29; 1.26	1.27/1.27	1.29	1.24	1.22; 1.33		1.21
$q_B(Co^T)$/|e|	+1.22	+1.22	+1.21		+1.20	+1.09	
$q_B(Co^O)$/|e|	+1.32	+1.31/+1.31	+1.36	+1.37		+1.34	
$q_B(N)$/|e|	+0.55	+0.52	+0.51	+0.42	+0.51		+0.70
$q_B(O)$/|e|	−0.61 −0.51	−0.49 −0.50	−0.57 −0.57	−0.44 −0.44	−0.67 −0.41		−0.35
$q_B(NO_2)$/|e|	−0.57	−0.47	−0.63	−0.46	−0.57		
$\mu(Co^T)/\mu_B$	2.58	2.57	2.59	2.48	2.54	2.55	
$\mu(Co^O)/\mu_B$	−0.02	−0.02	1.85			1.88	
$\mu(N)/\mu_B$	0.00	0.00	0.02	0.01	−0.03		0.26
$\mu(O)/\mu_B$	0.00 0.04	0.01 0.01	0.05 0.05	0.00 −0.02	0.05 −0.04		0.24

[a]The negative sign in the magnetization results from β spin orientation.

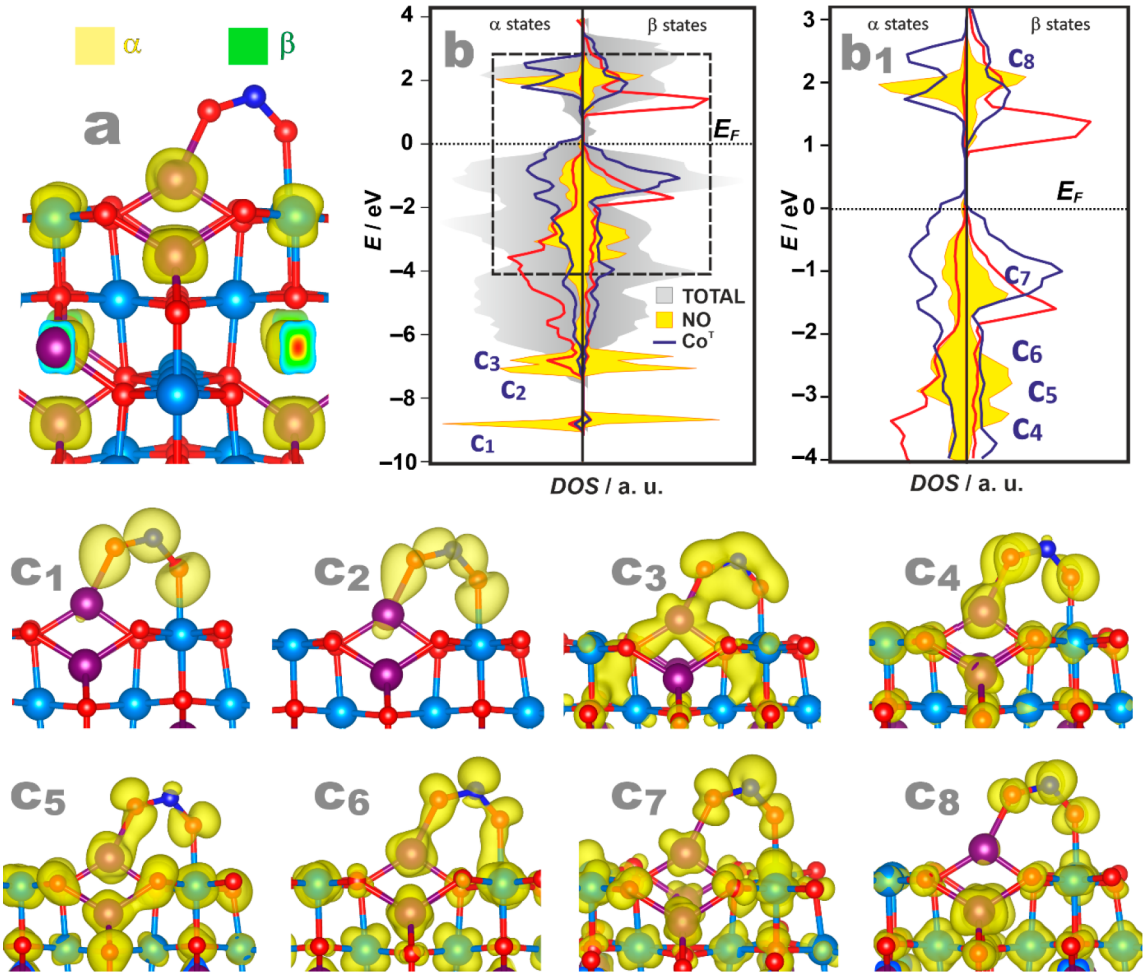

Figure 3. Spin density contour for the μ-η^1:η^1-Co^T–ONO–Co^O adduct (a), together with the profiles of density of states (b, b_1), and the corresponding most relevant partial charge density contours (c_1–c_8). Color coding: Co^T_{2c}, purple; Co^O_{5c}, light blue; N, dark blue; and O, red.

μ-η^1(O):η^1(N)-Co^T–O(O)N–Co^O NO_2 adducts of NO_2. This issue is further discussed in section 3.6.

From the structural characteristics of the associative NO_2 adsorption forms presented in Table 1, we learn that the N–Co and O–Co bonds are distinctly longer than in the case of NO and that the N–O bond is also slightly expanded upon coordination. The adsorption is accompanied by significant charge flow onto the NO_2 admolecule, and the electron density

https://dx.doi.org/10.1021/acs.jpcc.0c06195
J. Phys. Chem. C 2020, 124, 19681−19697

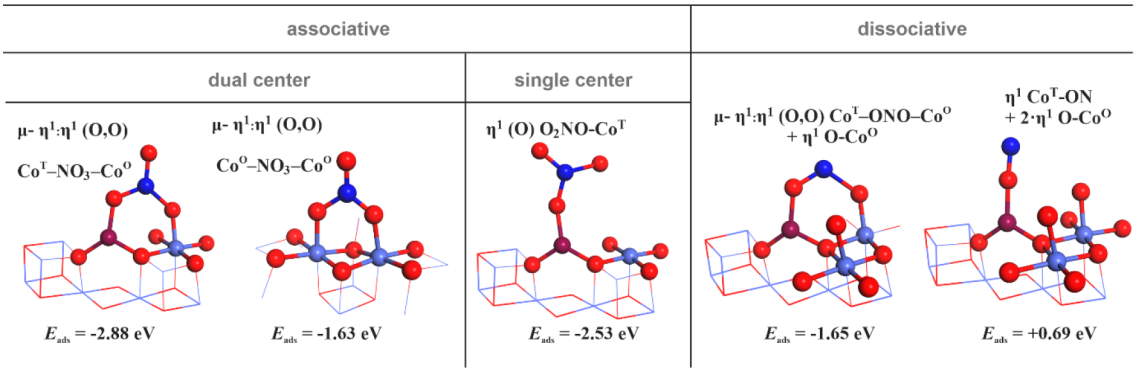

Figure 4. Conceivable associative and dissociative modes of NO_3 adsorption on the (100) surface of cobalt spinel together with the corresponding adsorption energies (E_{ads}). Color coding: Co^{T}_{2c}, purple; Co^{O}_{5c}, light blue; N, dark blue; and O, red.

Table 2. Energetics, Geometry, Partial Charge (q_B), and Magnetization (μ) of the Most Stable Associative Modes of NO_3 Adsorption on the (100) Termination of Cobalt Spinel, Together with the Reference Values Calculated for the Bare Spinel Surface and Gas-Phase $NO_{3(g)}$

	adsorption modes			reference states	
property	μ-η^1:η^1-Co^T–NO_3–Co^O	η^1-NO_3–Co^T	μ-η^1:η^1-Co^O–NO_3–Co^O	(100)-S	$NO_{3(g)}$
E_{ads}/eV	−2.88	−2.53	−1.63		
d_{Co-NOx}/Å	1.90; 2.09	1.84	1.95; 1.99		
d_{N-O}/Å	1.33; 1.22	1.39; 1.23	1.30; 1.23		1.25
$q_B(Co^T)$/|e|	+1.24	+1.23	+1.13	+1.09	
$q_B(Co^O)$/|e|	+1.35	+1.38	+1.36	+1.34	
q_B(N)/|e|	+0.83	+0.84	+0.82		+0.90
	−0.62	−0.64	−0.51		
q_B(O)/|e|	−0.50	−0.64	−0.40		−0.30
	−0.37	−0.42	−0.40		
$q_B(NO_3)$/|e|	−0.65	−0.86	−0.49		0.00
$\mu(Co^T)/\mu_B$	2.59	2.56	−2.55	2.55	
$\mu(Co^O)/\mu_B$	−0.01	1.85	0.03	1.88	
μ(N)/μ_B	0.00	0.00	0.00		−0.03
	0.05	0.10	0.00		
μ(O)/μ_B	0.01	0.01	0.00		+0.29
	0.01	0.01	0.00		

is not shared equally between the atoms. A pronounced negative charge acquired by the NO_2 adspecies (Δq_B is ranging from −0.46 to −0.63 |e| for different adsorption modes) and their apparently closed-shell nature ($\mu_{NO_2} \cong 0$, see the bottom rows in Table 1) are in line with a NO_2^- formulation of the ligated molecule. Analysis of the electronic and magnetic structure of the surrounding cobalt cations did not reveal any specific Co^O electrodonor center, in contrast to the Co^T sites that exhibit a distinct charge increase. However, a significant drop in the magnetization from μ = 1.88 μ_B to $\mu \cong 0$ μ_B observed for the Co^O_{5c} cations can be associated with the $t_{2g}^5e_g^1 \rightarrow t_{2g}^6e_g^0$ spin-crossover into the diamagnetic state induced by the NO_2 ligation.

The spin density repartition for the most stable μ-η^1:η^1-Co^T–ONO–Co^O exemplary adduct is shown in Figure 3a, and the associated partial charge density maps along with the *p*DOS plots are presented in Figure 3b,c, respectively. Inspection of Figure 3a confirms that only the Co^T moiety maintains its paramagnetic state upon the NO_2 ligation. A more thorough insight into the coordination features of the bridging NO_2 attachment was obtained from the detailed examination of the DOS structure and the partial charge density diagrams for the most relevant ligand–metal MO interactions (Figure 3b,c). Analysis of the hybridization extent of the key σ and π/π^* orbitals of NO_2 with the 3*d* orbitals of the Co^T and Co^O cations shows strongly uneven involvement of both cobalt centers in the NO_2 ligation. Hybridization of the deep-lying $4a_1$, $3b_1$ (and $1b_2$) with the 3d Co orbitals is negligible (see Figure 3c_1,c_2), and the corresponding DOS states are located in the range from −6.5 to −9 eV (Figure 3b). Strong in-plane and out-of-plane π–3d interactions that are essential for the NO_2 binding are highly spin-polarized, and associated with the DOS features located in the band between −5 and −1 eV. The in-plane $5a_1$–d_{xz}, $4b_1$–d_{z^2}/d_{xz} and the $1a_2$–d_{yz} out-of-plane bonding interactions may serve as a lucid illustration of the uneven involvement of both cobalt sites in the NO_2 ligation (Figure 3c_3,c_4,c_5). In contrast, the originally SOMO orbital ($6a_1$) is strongly, and more equally, hybridized with the $3d_{xz}$ orbitals of the dual Co^T and Co^O centers (see Figure 3c_6 for bonding and Figure 3c_7 for the antibonding interactions), giving rise to the DOS features located between −0.5 and −1.5 eV below E_F, in accordance with the NO_2^- formulation of the ligated nitrogen dioxide. In turn, the empty $2b_2$ MO of the NO_2 moiety is only weekly hybridized with cobalt 3d; thus, it can be associated with the dominant DOS state located above the Fermi level.

https://dx.doi.org/10.1021/acs.jpcc.0c06195
J. Phys. Chem. C 2020, 124, 19681−19697

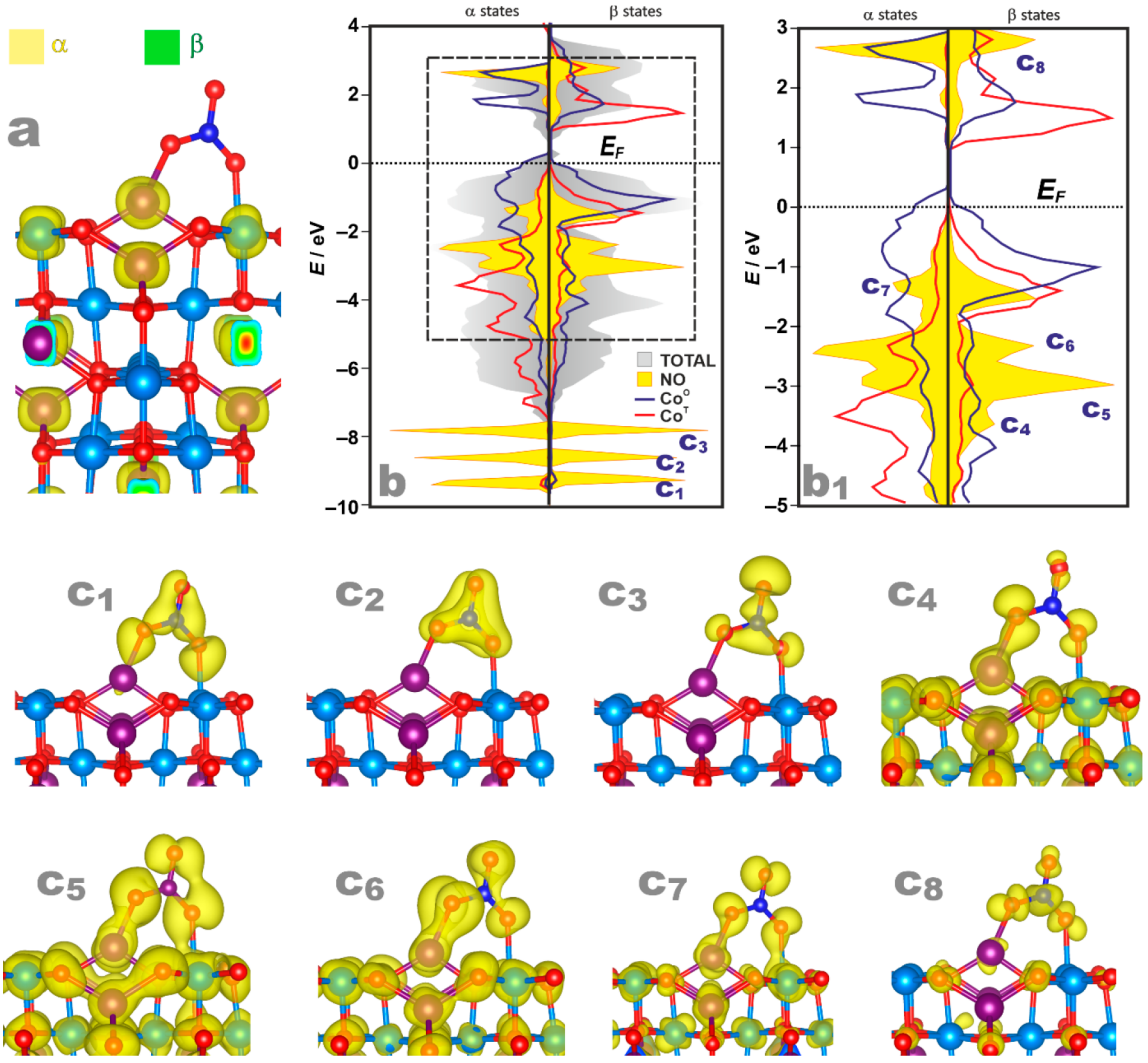

Figure 5. Spin density contour of the μ-η^1:η^1-Co^T−ONO_2−Co^O surface adduct (a), together with the profiles of density of states (b, b_1), and the corresponding most relevant partial charge density contours (c_1−c_8). Color coding: Co^T_{2c}, purple; Co^O_{5c}, light blue; N, dark blue; and O, red.

3.3. NO_3 Adsorption. Once NO_2 is adsorbed (or formed) on the surface of the catalyst, it can readily recombine with an adjacent oxygen adatom to generate nitrogen trioxide species ($NO_{2(ads)} + O_{(ads)} \rightarrow NO_{3(ads)}$).[63−65] Thus, for a comprehensive account of the surface nitrogen oxides description, adsorption of NO_3 on the cobalt spinel (100) termination was also examined. The adducts resulting from the associative and dissociative adsorption modes of a NO_3 moleculeare shown in Figure 4, together with the calculated E_{ads} values. Due to the high symmetry of the NO_3 molecule (D_{3h}), the surface binding scenarios were substantially reduced in comparison with the previously described NO_2 varieties.

The μ-η^1(O):η^1(O) bridging adducts, Co^T−(ONO_2)−Co^O and Co^O−(ONO_2)−Co^O, are characterized by the adsorption energies of −2.88 and −1.63 eV, respectively. Such a large energy difference again reveals that the exposed diagonal Co^T_{2c} cations exhibit much higher affinity to bind NO_x species than the more coordinatively saturated Co^O_{5c} sites. This finding is also valid for a monodentate O_2NO−Co^T adduct, whose adsorption energy (E_{ads} = −2.53 eV) is even higher (in absolute value) than that calculated for the doubly bonded Co^O−(ONO_2)−Co^O complex (E_{ads} = −1.63 eV). Two most probable dissociative modes of the NO_3 adsorption are presented in the fourth column in Figure 4. Breaking one of the N−O bonds leads to the formation of μ-η^1(O):η^1(O)-Co^T−ONO−Co^O and O−Co^O_{5c} adspecies (described in detail in Figure 2 and Table 1), whereas breaking of the second N−O bond gives rise to a NO molecule attached through the oxygen atom to the Co^T_{2c} center. Only in the former case is the resultant dissociative configuration stable against gas-phase NO_3 (E_{ads} = −1.65 eV). It is, however, definitely less stable than the associatively adsorbed μ-η^1(O):η^1(O)-Co^T−(ONO_2)−Co^O adduct (E_{ads} = −2.88 eV). Dissociatively adsorbed NO_3 is kinetically stable only and may likely be converted back into the molecular NO_3 adspecies. Double dissociation of the NO_3 adducts is definitely unfavorable due to the positive energy of this process (E_{ads} = +0.69 eV).

Analysis of the data presented in Table 2 reveals that the interfacial coordination chemistry of NO_3 on the (100) Co_3O_4 surface is in gross features similar to that observed for NO_2. In all cases, owing to the high electron affinity of NO_3, its adsorption is accompanied by significant charge flow from the spinel surface onto the ligand, leading to the formation of a negatively charged closed-shell NO_3^- species (see the bottom rows of Table 2). The most stable μ-η^1:η^1-Co^T−ONO_2−Co^O adduct is characterized by a bond length of d_{Co^T-ON} = 1.90 Å

https://dx.doi.org/10.1021/acs.jpcc.0c06195
J. Phys. Chem. C 2020, 124, 19681−19697

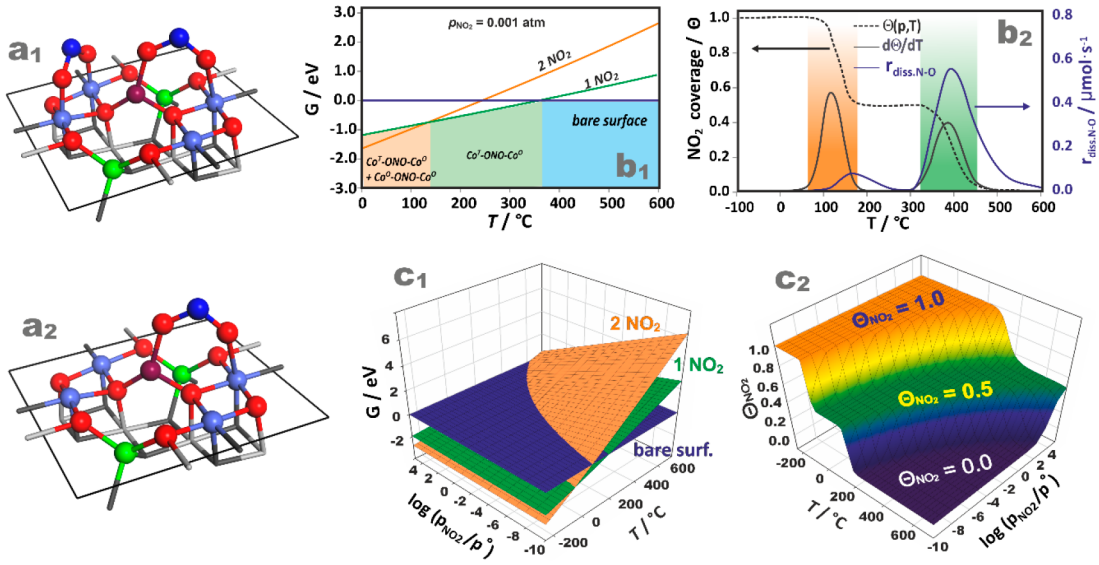

Figure 6. (a) Cobalt spinel (100) surface element covered with one (a_1) and two (a_2) NO_2 molecules. Gibbs free energy of NO_2 adsorption as a function of temperature for p_{NO_2} set to 500 ppm (b_1), together with the corresponding Θ_{NO_2} vs T, $d\Theta/dT$ vs T, and $r_{diss.N-O}$ vs T profiles (b_2). 3D Gibbs free energy diagrams of NO_2 adsorption (c_1) and the resulting surface coverage 3D diagram for a wide range of temperatures and NO_2 pressures (c_2).

and d_{CoO-ON} = 2.09 Å. The charge flow from the surface into the NO_3 admolecule was equal to −0.65 |e| that with the null value of the magnetization ($\mu_{NO_3} \cong 0$) implies an electron donation from the surface into the SOMO of NO_3 to produce a closed shell NO_3^- ligand. Only small alterations in the oxidation state of the hosting sites were observed (Δq_B (Co^T_{2c}) = +0.15 |e| and Δq_B (Co^O_{5c}) = −0.01 |e|). However, a significant drop of the magnetization takes place at the Co^O_{5c} center (from 1.88 μ_B to 0 μ_B). The resultant spin density contour for this adsorption mode is shown in Figure 5a, where the electrons are paired in both the admolecule and the Co^O_{5c} hosting site as well. The *p*DOS structure and the corresponding partial charge density maps are presented in Figure 5b,b_1,c_1−c_5, respectively. The deep $1b_1$, $2a_1$, $2b_1$ states (labeled within the C_{2v} symmetry) remain practically intact (Figure 5c_1−c_3), contributing to the DOS features in the range from −10 to −8 eV. (Figure 5b). The bonding interactions are located in the energy region from −5 eV to the Fermi level edge (Figure 5b_1). They result from the strong in-plane and out-of-plane interactions of the $3a_1$, $3b_1$, $4b_1$, $1b_2$ and $5b_1$ states of NO_3 with the corresponding d_{z^2}/d_{xz} (in-plane) and d_{yz} (out of plane) states of the cobalt sites (Figure 5c_4−c_7). The LUMO $2b_2$ orbital of NO_3 interacts rather weekly with its Co 3d counterpart, bringing about a first intense empty band at 1.5 eV in the DOS structure (Figure 5b_1). In summary, the performed analysis of the NO_3 ligation reveals that the nitrogen trioxide molecule is inequitably attached to the cobalt spinel (100) surface, where the exposed Co^T cations play the key role in the binding process.

3.4. *Ab Initio* Thermodynamics of the NO_2 and NO_3 Adsorption. Once the NO_2 and NO_3 adsorption forms on the (100) plane were systematically delineated, we applied the atomistic thermodynamic modeling to examine surface coverage variation as a function of the temperature and partial pressure ($\Theta(p, T)$).

In Figure 6a_1,a_2 show different NO_2 coverages corresponding to $\Theta_{NO_2} \approx 1.51$ molecule·nm^{-2} and Θ_{NO_2} = 3.02 molecule·nm^{-2}, respectively. The lower coverage is associated with the most stable bridging μ-η^1(O):η^1(O)-Co^T−ONO−Co^O adducts, whereas the higher coverage corresponds to the additional adsorption of another NO_2 molecule on the adjacent dual [Co^O_{5c}···Co^O_{5c}] site in the μ-η^1(O):η^1(O)-Co^O−ONO−Co^O configuration. The calculated repulsion forces between both admolecules are equal to 0.25 eV. The remaining bare Co^O_{5c} adsorption site was not occupied by the third NO_2 molecule to reach higher coverage (4.53 molecule·nm^{-2}), as the repulsion forces overwhelm the adsorption energy by 0.2 eV. Both stable adsorption models were next used to calculate the free enthalpy variation for the (100) surface covered by NO_2 as a function of temperature, for the reference NO_2 pressure set to p_{NO_2} = 0.001 atm (Figure 6b_1). The bottom envelope of the plot corresponds to the most stable adsorption scenario under given thermodynamic conditions. A brief analysis of the results reveals that the NO_2 monolayer (corresponding to 2 adsorbed NO_2 molecules) is stable below 100 °C, and the less-stable NO_2 molecule attached to the Co^O_{5c}···Co^O_{5c} sites is released. The temperature window of the surface stability for the μ-η^1(O):η^1(O)-Co^T−ONO−Co^O adduct (1NO_2 line) extends up to 380 °C, where upon its desorption a bare surface becomes the most stable state. For a more tangible description of the adsorption process, the corresponding surface coverage, $\Theta(p, T)$, along with its differential profile, $d\Theta/dT$, were also calculated (Figure 6b_2). The latter reveals the ranges of the most significant changes in the coverage as the temperature increases, which may be associated with the appearance of desorption maxima in the TPD profiles when quasi-equilibrium conditions are satisfied.[63] As shown in the $d\Theta/dT$ profile (solid gray line in Figure 6b_2), desorption of the first NO_2 molecule occurs at T = 110 °C, and it is characterized by a narrow $d\Theta(T)/dT$ peak (the full width at half-maximum fwhm = 50 °C). The release of the second NO_2 molecule gives rise to a much broader desorption peak (fwhm = 100 °C). Thus, the first portions of NO_2 may leave the surface at about 310 °C, due to thermal decomposition of the μ-η^1(O):η^1(O)-

https://dx.doi.org/10.1021/acs.jpcc.0c06195
J. Phys. Chem. C 2020, 124, 19681−19697

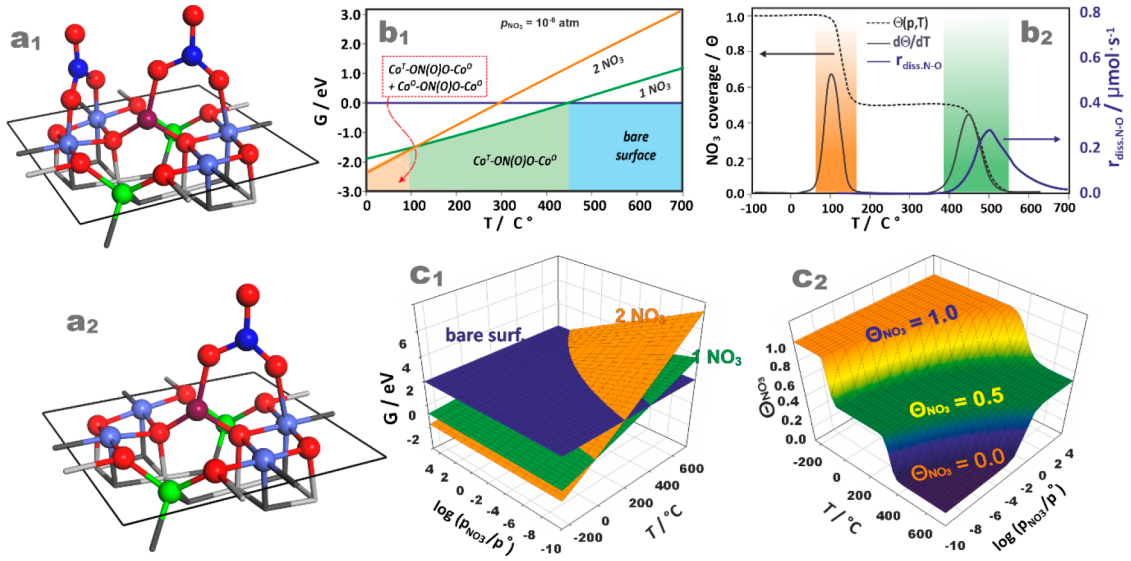

Figure 7. (a) Cobalt spinel (100) surface element covered with one (a_1) and two (a_2) NO_3 molecules. Gibbs free energy of NO_3 adsorption as a function of temperature for p_{NO_3} set to 10^{-6} atm. (b_1), together with the corresponding Θ_{NO_3} vs T, $d\Theta_{NO_3}/dT$ vs T, and $r_{diss.N-O}$ vs T profiles (b_2). 3D Gibbs free energy diagrams of NO_3 adsorption (c_1), and the resulting surface coverage 3D diagram for a wide range of temperatures and NO_3 pressures (c_2).

$Co^T-ONO-Co^O$ adduct, and the desorption process is extended to the temperature as high as 450 °C, where the last portions of NO_2 are released.

To assess the competition between the associative and dissociative desorption of NO_2 (described in detail in section 3.6), we also added a plot of temperature variation of the rate of the ON−O bond dissociation (Figure 6b_2, blue line), calculted as a first order process: $r(T) = k(T)\ \Theta_{NO_2}$, $k(T) = \frac{k_B T}{h} \exp\left(\frac{-\Delta G^{\#}}{RT}\right)$. The coverage was obtained from the atomistic thermodynamic modeling (*vide supra*), whereas the free energy of the activation was obtained from the DFT calculations including the entropic term derived from the harmonic vibrational analysis. For low temperatures, dissociation of the NO_2 adduct over $Co^O\cdots Co^O$ is triggered at about 100 °C and is shifted toward higher temperature by about 50 °C in comparison to thermodynamic direct associative desorption peak. This process is characterized by a rather small energy barrier of 1.16 eV (see below, Figure 10, step $\mathbf{a_1}$). The rate of dissociation reaches a maximum at about 175 °C, then a rapid decrease of the μ-η^1(O):η^1(O)-Co^O−ONO−Co^O coverage leads to a gradual decrease of the dissociation rate, until its eventual ceasing at 250 °C. These results reveal that direct desorption of NO_2 from the $Co^O\cdots Co^O$ sites occurs in a similar temperature window with the O−NO bond dissociation. After NO_2 dissociation the NO fragments are easily released at this temperatures, since NO is stabilized on the Co^O site by 0.49 eV only (see Figure S2). For the μ-η^1(O):η^1(O)-Co^O−ONO−Co^O adducts the dissociation process is shifted toward higher temperatures (in line with higher value of E_a = 1.68 eV, see Figure 9, step $\mathbf{a_1}'$). It starts about 300 °C (coincidentally in the same temperature as direct desorption), and it reaches a maximum at ∼400 °C. The dissociation peak is much more pronounced compared to its low temperature counterpart; thus, we may expect that the dissociative pathway plays a prime role in desorption of the NO_2 adducts stabilized on the $Co^O\cdots Co^T$ sites. In summary, the desorption of NO_2 is an involved process and may proceed by NO_2 or NO and O_2 release.

The overall thermodynamic diagram of the NO_2 adsorption (Figure 6c_1) provides a general view of the ΔG_{ads} changes with pressure and temperature. It may be transposed into a 3D diagram of the NO_2 coverage variation as a function of T and p_{NO_2} (Figure 6c_2). Inspection of this diagram shows that at low temperatures (T < 150 °C) the surface is blocked by the adsorbed NO_2 in the wide range of pressures. The temperature of the complete surface liberation is distinctly shifted to higher temperatures when NO_2 is more (up to 500 °C for p_{NO_2} = 1 atm) or less (down to 300 °C, for $p_{NO_2} = 10^{-6}$ atm) abundant in the feed (see Figure 6c_2).

Analogous modeling was performed for the NO_3 adsorption, and the surfaces covered with one ($Co^T-ONO_2-Co^O$) and two ($Co^T-ONO_2-Co^O$ and $Co^O-ONO_2-Co^O$) adspecies are presented in Figure 7a_1,a_2, respectively. However, since gaseous NO_3 is quite unstable, it is problematic to set a reliable real partial pressure range for this species. Therefore, for the thermodynamic modeling we set the virtual pressure of NO_3 to an arbitrary level of 10^{-6} atm. The free enthalpy variation for the (100) surface at various NO_3 coverage for $p_{NO_3} = 10^{-6}$ atm (Figure 7b_1) shows that the surface is fully covered by NO_3 below 100 °C. Above this temperature, the less stable $Co^O-ONO_2-Co^O$ adduct associated with the dual $Co^O_{5c}\cdots Co^O_{5c}$ site spontaneously decompose. The temperature window of the $Co^T-ONO_2-Co^O$ stability (1NO_3 line) extends up to 470 °C. These threshold temperatures are better manifested in the corresponding Θ_{NO_3} and $d\Theta_{NO_3}/dT$ vs T plots (Figure 7b_2). Desorption of the first NO_3 molecule occurs in the low-temperature region (50−150 °C), and it is described by a narrow $d\Theta/dT$ peak (fwhm = 55 °C), whereas thermal detachment of the second NO_3 molecule is ascribed by a substantially broader (fwhm = 140 °C) desorption peak. The diabatic associative desorption starts at about 380 °C, and the process extends up to 570 °C where the last portions of NO_3 are removed. The overall 3D thermodynamic diagram of the

https://dx.doi.org/10.1021/acs.jpcc.0c06195
J. Phys. Chem. C 2020, 124, 19681−19697

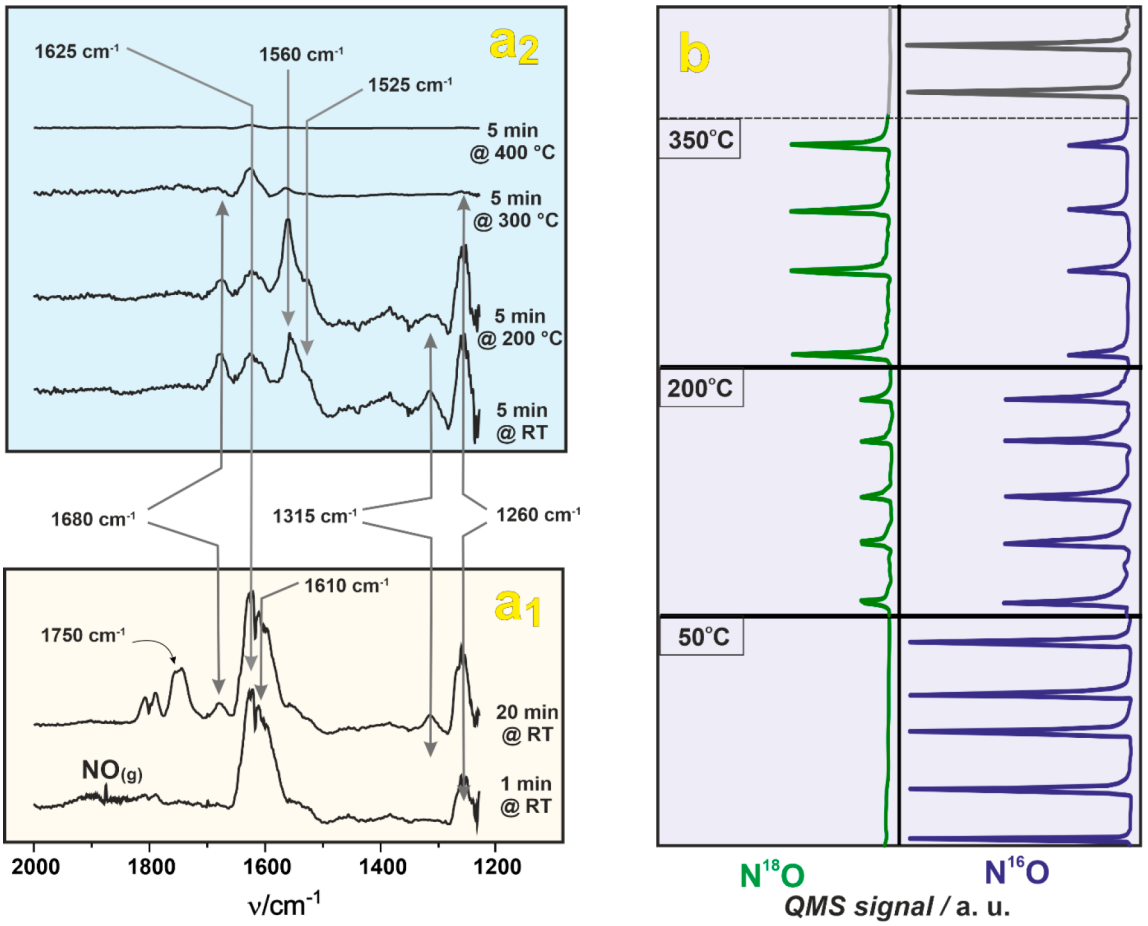

Figure 8. *In situ* FT-IR spectra of NO adsorption on oxygen covered (100) surface exposed by Co_3O_4 nanocubes (a_1) at room and (a_2) at elevated temperatures. A variable-temperature isotopic exchange pulse experiment of $N^{16}O$ interaction with the ^{18}O covered surface (b).

NO_3 adsorption (Figure 7c_1) was next transformed into the NO_3 coverage variation as a function of T and p_{NO_2} (Figure 7c_2). As can be inferred from the inspection of both diagrams, at the presumed pressures, the surface is totally blocked by adsorbed NO_3 below 100 °C. The bare surface is expected to appear in much higher temperatures, in comparison to NO_2, but only when the associative desorption conditions are maintained. This remains in line with higher adsorption energies of the NO_3 molecules (−2.88 eV versus −1.91 eV). In analogy to NO_2, removal of the $Co^O\cdots Co^O$ adsorbed NO_3 adspecies may actually occur along a dissociative pathway with a lower barrier, as discussed in section 3.6. However, for the assumed NO_3 pressure, direct desorption of $Co^O-ONO_2-Co^O$ adspecies takes place at temperatures T < 100 °C, thus a significant value of the activation energy for the N−O bond dissociation in NO_3 adspecies (E_{act} = 1.42 eV, see below Figure 11, step $\mathbf{b_2}'$) hinders its feasibility. Therefore, in contrast to NO_2 (Figure 6b_2), participation of dissociative NO_3 desorption is not expected, which is clearly revealed by absence of the peak in the $r(T)$ plot (blue line in Figure 7b_2) in the low-temperature region. For the more stable $Co^O-ONO_2-Co^T$ adducts, the dissociation barrier of 2.25 eV (see Figure 11, step $\mathbf{a_2}'$) shifts this process to 400 °C (50 °C higher than that expected for direct desorption); thus, the dissociation rate attenuated quickly by the decreasing coverage (reaching the maximum peak at 500 °C). Overlapping of the thermodynamic and kinetic peaks reveals that for the NO_3 adduct with the $Co^T\cdots Co^O$ sites a competition between the direct desorption and dissociative desorption shall be expected, similar to the NO_2 case (see Figure 6).

The results presented above reveal that both NO_2 and NO_3 molecules are strongly attached to the (100) surface of Co_3O_4. As a result, in the deN_2O reaction, at moderate temperatures (250 °C < T < 400 °C), the NO_2 and NO_3 molecules remain strongly connected to the surface, blocking the $Co^T_{2c}\cdots Co^O_{5c}$ cobalt active sites even at their very low abundances (log $p_{NO_2}/p_0 \cong -5$). This fact accounts nicely for the harmful effect of NO_x presence in the tail gases of nitric acid plants on the N_2O decomposition efficiency[66] or for high sensitivity of the Co_3O_4-based sensors to NO_2 detection.[41,42]

3.5. Spectroscopic IR and Isotopic Exchange Experiments. For verification of the obtained theoretical results, we performed corroborative IR investigations, using NO adsorption on the surface of cubic Co_3O_4 nanocrystals covered by oxygen, for *in situ* generation of the NO_2 and NO_3 adspecies (Figure 8a). Initially, after adsorption of the 10 Torr of NO under ambient conditions (Figure 8a_1) the characteristic peaks of the gaseous NO (1875 cm^{-1}), NO_2 (1650−1550 cm^{-1}), and N_2O_4 were detectable. Dinitrogen tetraoxide is obtained upon NO_2 dimerization, and its characteristic bands ($\nu_{as}(NO_2)$ at 1758−1730 cm^{-1} and $\nu_s(NO_2)$ at 1368−1359 cm^{-1}) are readily observed. In addition to gas-phase NO_2 and N_2O_4, sizable bands of the chemisorbed NO_3 (1625 and 1560 cm^{-1}) and NO_2 (1260 and 1525 cm^{-1}) also appear. Accordingly, a significant increase in the intensity of the characteristic NO_2 and NO_3 bands was observed in the spectrum collected after

https://dx.doi.org/10.1021/acs.jpcc.0c06195
J. Phys. Chem. C 2020, 124, 19681−19697

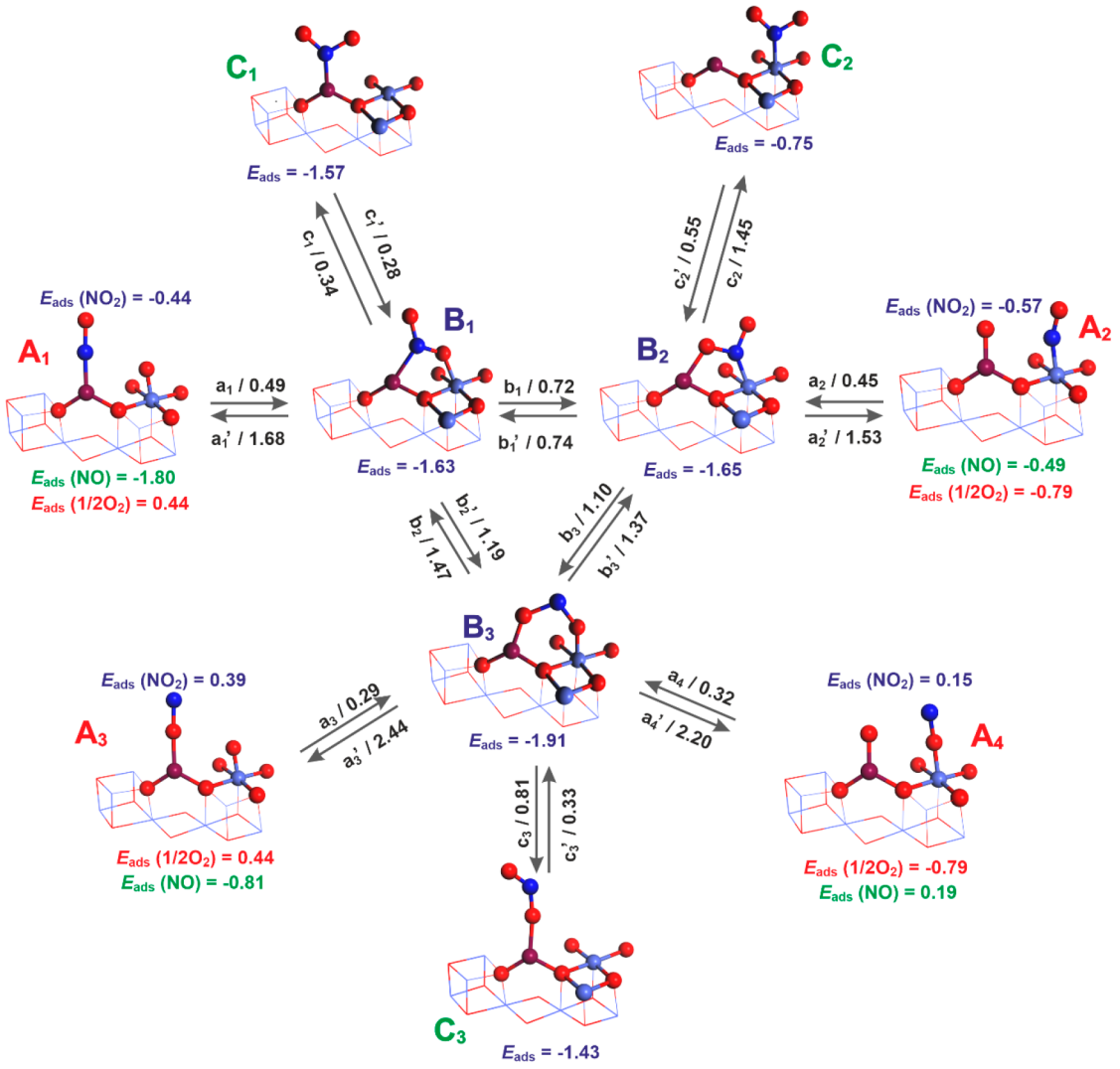

Figure 9. Pathways of the suprafacial NO ↔ NO_2 transformations over the $Co^T\cdots Co^O$ adsorption site on the cobalt spinel (100) surface. Structures $\mathbf{A_1}-\mathbf{A_4}$ illustrate the NO and O coadsorption, whereas structures $\mathbf{B_1}-\mathbf{B_3}$ and $\mathbf{C_1}-\mathbf{C_3}$ represent the bridging and monodentate modes of the NO_2 adsorption, respectively. Stabilization energies calculated with respect to a half of the gas phase O_2 are marked in red, and those with respect to gas NO are in green. The activation barriers of the forward and backward steps in black. Color coding: O, red; N, navy blue; Co^T_{2c} cobalt–violet; Co^O_{5c} cobalt–blue.

20 min of the NO exposure. It is worth mentioning that on the bare Co_3O_4 surface, NO is not spontaneously oxidized to NO_2 and NO_3 adspecies under such conditions.[65] The weakly bonded and gas-phase NO, NO_2, and N_2O_4 molecules are easily removed by evacuation (Figures 8a_2, bottom line), leaving the IR bands of the NO_2 and NO_3 surface adducts dominant. The bands at 1680, 1525, and 1315 cm^{-1} associated with the vibrations of the NO_2^- ligand can be assigned to the surface $Co^T-NO_2-Co^O$ and Co^T-NOO complexes and the chelating NO_2 adducts, respectively. The linkage isomers of NO_2 are revealed by the bands at 1260 and 1525 cm^{-1} due to the O- and the N-coordinated ligands, respectively. These NO_2 adspecies accumulate with time, accompanied by the appearance of the bands at 1625 and 1560 cm^{-1} due to the bound NO_3^-. Judging upon their stability in the temperature range of 100–400 °C, the 1625 cm^{-1} band can be associated with bridging $Co^T-NO_3-Co^O$ adducts, whereas the 1560 cm^{-1} band with the mono Co^T-NO_3 adducts.[67]

All such adducts were predicted to be stable by molecular modeling (see Figures 2 and 4). These results reveal that in line with theoretical predictions NO in the presence of the reactive oxygen species is readily oxidized into NO_2 and NO_3 forms even at low temperatures, and these adspecies may coexist adopting different conformations due to the comparable adsorption energies. Their relative abundance may also be governed by different formation mechanism (see below, section 3.6). Such a picture is essentially preserved upon heating to 200 °C, which is in accordance with the predicted thermal stability of both NO_2 and NO_3 admolecules (Figure 6 and 7). However, at 300 °C the bands assigned to NO_2 adspecies are significantly reduced, whereas the NO_3 bands persist and become nearly depleted at 400 °C only (top spectrum in Figure 8a_2).

Thus, the IR results are in accordance with the predicted thermal stability of the NO_2 species for low p_{NO_2} conditions (see Figure 6b_2), where NO_2 desorption is expected to occur just below 400 °C. For the NO_3 surface adducts, however, a diabatic direct $NO_{3(ads)} \rightarrow NO_{3(gas)}$ detachment is anticipated to occur at much higher temperatures (around 600 °C, see Figure 7b_2). As already mentioned, such species may be

https://dx.doi.org/10.1021/acs.jpcc.0c06195
J. Phys. Chem. C 2020, 124, 19681–19697

removed from the surface along an indirect, and energetically more expedient, stepwise mechanism that involves breaking of one of the N−O bonds of the NO_3 molecule with the concomitant formation of the surface NO_2 and O species ($NO_{3(ads)} \rightarrow NO_{2(ads)} + O_{(ads)}$). Such a mechanism is described in the next section in detail, and the resulting adspecies may desorb independently ($NO_{2(ads)}$ directly and $O_{(ads)}$ via diffusive recombination into $O_{2(g)}$)[68] at temperatures below 400 °C, in accordance with the spectroscopic observations.

The feasibility of a straightforward N−O bond making and breaking processes was next ascertained by pulse isotopic exchange experiments (Figure 8b), where $N^{16}O$ was adsorbed in a pulse fashion on the (100) surface covered by ^{18}O-labeled oxygen. A strong isotopic exchange between $^{18}O_{(ads)}$ and $N^{16}O$ occurs already above 200 °C, as can be inferred from the simultaneous presence of the $N^{16}O$ and $N^{18}O$ isotopomers in the gas phase. The $N^{18}O/N^{16}O$ ratio in the gas phase increases with the temperature, but surprisingly, the $N^{18}O$ isotopomer was always prevailing in the products, despite $N^{16}O$ being used. This result suggests the operation of an isotopic exchange mechanism, which involves alternate breaking of the N−O bonds in the $^{16}O-N-^{18}O$ intermediate ($NO_{2(ads)}$), formed by the association of the adsorbed $N^{16}O$ with the surface ^{18}O reactive species. Such bond breaking may produce both $N^{16}O$ and $N^{18}O$ isotopomers following the reaction:

$$\mathrm{Co{-}(O^{16}{-}N{-}O^{18}){-}Co} \longrightarrow \mathrm{Co{-}N^{16}O_{(g)} + Co{-}{}^{18}O}$$
$$\searrow \quad \mathrm{Co{-}N^{18}O_{(g)} + Co{-}{}^{16}O}$$

The scrambling is expected to be favored over the dual $Co^{O}_{5c}\cdots Co^{O}_{5c}$ sites.

3.6. Surface Dynamics of the NO_x Adspecies. For the comprehensive description of the observed intermolecular surface dynamics of the O ↔NO ↔ NO_2↔ NO_3 conversion, we calculated transition states and the energy barriers of the most relevant steps of the examined surface processes. The entropic terms were not considered explicitly here, since for the surface-confined events such contributions are relatively small in comparison to the dominant energy terms, as they also mutually cancel to a large extent.[69] Taking into account the large number of possible elementary steps, we discussed the NO ↔ NO_2 and NO_2 ↔ NO_3 conversions separately. The proposed molecular course of the NO ↔ NO_2 transformation over the dual $Co^{T}\cdots Co^{O}$ site is presented in Figure 9, where for each step the energy barriers (expressed in eV and marked in black) are indicated. For all considered surface adducts, the adsorption energies are calculated against that of gas-phase NO_2 (these values are colored in blue). In the case of dissociatively adsorbed NO_2, stabilization of both moieties is additionally shown, for the NO fragment with respect to the NO_{gas} energy (marked in green) and for the O adatom with respect to a half of the energy of the O_2 molecule (marked in red).

Structures $\mathbf{A_1}-\mathbf{A_4}$ show the coexistence of the $NO_{(ads)}$ and $O_{(ads)}$ adspecies in different configurations, which may result from dissociative adsorption of NO_2. Such structures may also be taken as a starting point for the one-step on-surface production of the bridging NO_2 adducts of various linkage isomerism ($\mathbf{B_1}-\mathbf{B_3}$). The N−O bond formation is represented by steps $\mathbf{a_1}-\mathbf{a_4}$, whereas the N−O bond dissociation is described by reverse steps $\mathbf{a_1}'-\mathbf{a_4}'$. The calculated energy barriers reveal that in each case formation of the associatively bound NO_2 species from the corresponding fragments is facile (the corresponding E_a values are in the range of 0.29−0.49 eV). Such findings are in line with the experimental IR observation that NO_2 bands appear immediately upon NO is contacted with the oxygen covered spinel surface, even at ambient temperatures (see Figure 8a). In contrast, a reverse reaction of the NO_2 adduct decomposition (back into $O_{(ads)}$ and $NO_{(ads)}$ species) is always much more demanding, as the calculated E_a values are situated between 1.45 to 2.44 eV). This discrepancy may be accounted for by large difference in the stability between the associative and dissociative NO_2 adsorption modes (Figure 2).

Associative NO_2 adsorption forms $\mathbf{B_1}-\mathbf{B_3}$ can be transformed quite easily into each other (see steps $\mathbf{b_1}-\mathbf{b_3}$ and $\mathbf{b_1}'-\mathbf{b_3}'$). The μ-η^1(O):η^1(N) adducts, $Co^{T}-NO_2-Co^{O}$ ($\mathbf{B_1}$) and $Co^{T}-O_2N-Co^{O}$ ($\mathbf{B_2}$), are separated by the medium barriers (around 0.7 eV), whereas their transformation into the most stable μ-η^1(O):η^1(O) $Co^{T}-NO_2-Co^{O}$ surface complex ($\mathbf{B_3}$) is distinctly more demanding (E_a = 1.10 and 1.19 eV). The bridging NO_2 ligand in all complexes has to overcome the energy barrier of 1.63−1.91 eV to be diabatically released without dissociation. The NO_2 liberation may instead occur via a less demanding two-step pathway that is featured by breaking of the one bond only. Such mechanism is launched following one of steps $\mathbf{c_1}-\mathbf{c_3}$, which all lead to the monodentate ligation of NO_2 in different configurations ($\mathbf{C_1}-\mathbf{C_3}$ structures). These steps differ in the activation energy, depending on the actual starting adduct and the nature of the bond that is broken. For the μ-η^1(N):η^1(O)-$Co^{T}-N(O)O-Co^{O}$ complexes ($\mathbf{c_1}$ step), the dissociation barrier of the $Co^{O}-O$ bond breaking is equal to only 0.34 eV, whereas when the $Co^{T}-O$ bond is cleaved (pathway $\mathbf{c_2}$), this barrier increases to 1.45 eV. In the case of the μ-η^1(O):η^1(O)-$Co^{T}-ONO-Co^{O}$ adduct ($\mathbf{B_3}$), the activation energy of the $Co^{T}-O$ bond breaking (step $\mathbf{c_3}$) exhibits an intermediate value of 0.81 eV. The resultant monodentate species ($\mathbf{C_1}-\mathbf{C_3}$) are also unevenly stabilized. The C^{T}_{2c} attached NO_2 complexes ($\mathbf{C_1}$ and $\mathbf{C_3}$) which are more easily built are still strongly bonded (E_{ads} of 1.57 and 1.43 eV, respectively), whereas the less stabilized adduct (0.75 eV), $\mathbf{C_2}$, with NO_2 attached to Co^{O}_{5c} is characterized by significantly lower adsorption energy. All three established pathways of the NO_2 desorption from the $Co^{T}\cdots Co^{O}$ dual sites are featured by significant activation barriers. In the case of the $\mathbf{B_1}-\mathbf{C_2}$ and $\mathbf{B_3}-\mathbf{C_3}$ routes, the desorption is disfavored by the high adsorption energies of the monodentate NO_2 species, whereas for the $\mathbf{B_2}-\mathbf{C_2}$ pathway, it is disfavored by the high barrier of the O−NO bond breaking. Thus, NO_2 desorption from the $Co^{T}\cdots Co^{O}$ dual sites is not expected to take place readily at low and moderate temperatures.

Summarizing, analysis of the interfacial dynamics of the NO_x adspecies stabilized on the dual $Co^{T}\cdots Co^{O}$ sites shows that they are easily formed and are stable up to T > ∼400 °C (see Figure 6). Thus, the $Co^{T}\cdots Co^{O}$ sites being blocked in the temperature range when the NO → NO_2 oxidation is observed[40] cannot constitute efficient active centers for the NO oxidation reaction and cannot play any significant role in the experimentally observed isotopic $N^{18}O/N^{16}O$ scrambling as well (Figure 8b).

The situation is significantly different for the dual $Co^{O}\cdots Co^{O}$ sites that accommodate NO_2 at the distinctly lower extent. From the thermodynamic considerations, we can expect that such sites are bare at temperatures above 150 °C (see Figures 6b and 7b) and may be responsible for the catalytic activity of

https://dx.doi.org/10.1021/acs.jpcc.0c06195
J. Phys. Chem. C 2020, 124, 19681−19697

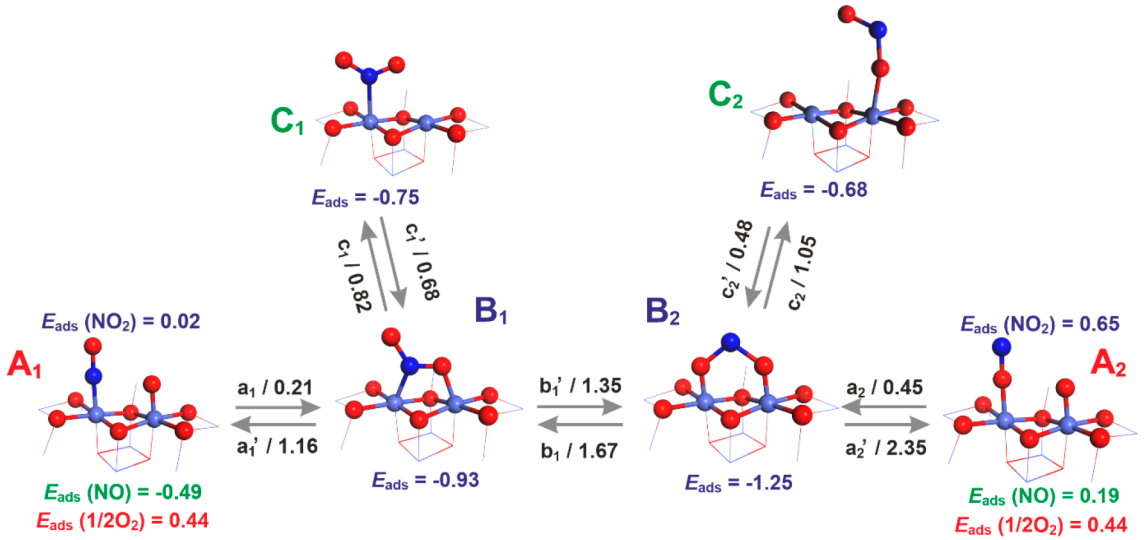

Figure 10. Pathways of the suprafacial NO ↔ NO_2 transformation over the Co^O···Co^O adsorption site on the cobalt spinel (100) surface. Structures $\mathbf{A_1}$ and $\mathbf{A_2}$ depict NO and O coadsorption, whereas structures $\mathbf{B_1}$ and $\mathbf{B_2}$ and $\mathbf{C_1}$ and $\mathbf{C_2}$ represent bridging and monodentate modes of NO_2 adsorption, respectively. Stabilization energies calculated with respect to half of the gas phase O_2 are marked in red, and those with respect to gas NO are in green. The activation forward and backward barriers in black. Color coding: O, red; N, navy blue; Co^T_{2c} cobalt−violet; Co^O_{5c} cobalt−blue.

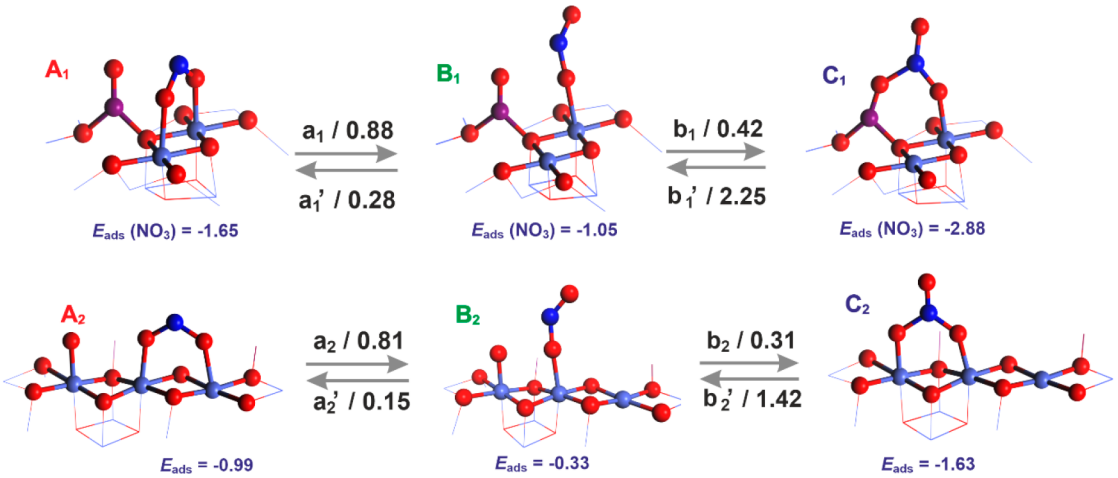

Figure 11. Pathways of the suprafacial NO_2 ↔ NO_3 transformation over the Co^O···Co^T (top panel) and Co^O···Co^T (bottom panel) adsorption sites on cobalt spinel (100) surface. Structures $\mathbf{A_1}$ and $\mathbf{A_2}$ depict NO_2 and O coadsorption. Structures $\mathbf{B_1}$ and $\mathbf{B_2}$ refer to reaction intermediates with monodentate NO_2 adspecies, whereas $\mathbf{C_1}$ and $\mathbf{C_2}$ represent bridging modes of NO_3 adsorption. The activation energies of the forward and backward steps marked in black. Color coding: O, red; N, navy blue; Co^T_{2c} cobalt−violet; Co^O_{5c} cobalt−blue.

the NO oxidation and $N^{18}O/N^{16}O$ scrambling reactions. As shown in Figure 10, the number of possible molecular events is significantly reduced comparing with the Co^O···Co^T pair centers. Again, the dissociative adsorption of NO_2 ($\mathbf{A_1}$ and $\mathbf{A_2}$ structures) is energetically much less favorable than the associative one ($\mathbf{B_1}$ and $\mathbf{B_2}$). Thus, the on-surface N−O bond formation is thermodynamically favored, and the barriers of such process are quite small ($\mathbf{a_1}$ = 0.21 eV and $\mathbf{a_2}$ = 0.45 eV; see Figure 10). The associatively adsorbed bridging adducts ($\mathbf{B_1}$ and $\mathbf{B_2}$) may mutually be transformed into each other, but with rather large barriers of 1.35 and 1.67 eV, respectively (see steps $\mathbf{b_1}$ and $\mathbf{b_1}'$). Breaking of the N−O bond in the bridging conformations ($\mathbf{B_1}$ and $\mathbf{B_2}$) that may initiate the NO_2 desorption route, requires 0.82 and 1.05 eV for steps $\mathbf{c_1}$ and $\mathbf{c_2}$ to proceed, respectively. However, compared to the dual Co^T···Co^O sites, the monodentate NO_2 ligand is less tightly bound (−0.75 and −0.68 eV versus −1.65 or −1.91 eV), and it may thereby be released at lower temperatures. Such a situation is beneficial for low-temperature catalytic oxidation of NO which, in fact, is experimentally observed to occur slightly above 200 °C. A more detailed inspection of the NO↔ NO_2 transformation reveals also a plausible mechanism of the observed isotopic scrambling (see Figure 8b). It is clear that dissociation of the NO_2 adducts back into the $NO_{(ads)}$ and $O_{(ads)}$ components is more demanding than the N−O bond formation. The barrier for the NO_2 dissociation in the μ-η^1(O):η^1(O) Co^O−ONO−Co^O adduct ($\mathbf{B_2}$) is significant ($\mathbf{a'}_2$ = 2.35 eV), making such process feasible only at elevated temperatures, well above the temperature window for the direct associative NO_2 desorption. Thus, this route it is substantially hindered and can not account for the experimental isotopic exchange results. The second μ-η^1(O):η^1(N)-Co^O−O(O)N−Co^O adduct ($\mathbf{B_1}$) exhibits the smaller barrier of 1.16 eV ($\mathbf{a'}_1$ step) to dissociate NO_2, which is

https://dx.doi.org/10.1021/acs.jpcc.0c06195
J. Phys. Chem. C 2020, 124, 19681−19697

comparable to the NO_2 adsorption energy. Thus, both processes of associative NO_2 desorption and NO_2 dissociation may occur concurrently (see also Figure 6b_2). The second is, therefore, responsible for the $N^{18}O$ $-N^{16}O$ isotopic scrambling. For this purpose, the involvement of monodentate adduct $\mathbf{C_1}$ as an intermediate is necessary. Indeed, once the bridging NO_2 adduct is formed ($\mathbf{B_1}$), it may turn into $\mathbf{C_1}$ by breaking a Co−O bond with the relatively small activation energy of E_a = 0.82 eV (step $\mathbf{c_1}$). The resultant monodentate O_2N-Co^O complex may release the NO_2 ligand (E_{des} = 0.75 eV), delineating the final step of the NO to NO_2 oxidation. Alternatively, by employing the "left" or "right" oxygen atom it may be rebound to the bare Co^O site to restore the μ-η^1(O):η^1(N)-Co^O−O(O)N−Co^O adduct ($\mathbf{c_1}'$) with E_a of 0.68 eV only. The doubly bonded μ-η^1(O):η^1(N)-Co^O−ONO−Co^O may, in turn, dissociate to NO and O adspecies. Taking into account that NO is stabilized on the Co^O site by only 0.49 eV, its desorption may compete successfully with the restoration of the bridging adspecies ($\mathbf{B_1}$), thanks to the substantial gain in the entropy owing to $NO_{(g)}$ release (such labile molecules are expected to liberate surface at temperatures below 0 °C, even at rather high pressures of NO (0.01 atm), see Figure S6). As a result, the $\mathbf{A_1} \leftrightarrow \mathbf{B_1} \leftrightarrow \mathbf{C_1}$ pathway plays a pivotal role in the mechanism of the $N^{16}O/N^{18}O$ isotopic exchange and the NO to NO_2 oxidation reactions and their mutual trade-off as well.

The molecular route of the on-surface transformation of NO_2 into NO_3 over the $Co^T\cdots Co^O$ and $Co^T\cdots Co^O$ dual centers is shown in Figure 11. In both cases, the lowest activation energy was found for the two-step process with formation of a monodentate intermediate. The $\mathbf{A_1} \rightarrow \mathbf{B_1} \rightarrow \mathbf{C_1}$ sequence presented in the top panel of Figure 11 illustrates such mechanism for the $Co^T\cdots Co^O$ sites. It begins by involving the Co^T-O and μ-η^1(N):η^1(O)-Co^O−ONO−Co^O adducts ($\mathbf{A_1}$) and requires a moderate activation energy of 0.88 eV for the Co^O-N bond breaking to occur ($\mathbf{a_1}$). The resultant η^1(O)-Co^O−ONO top-on adduct ($\mathbf{B_1}$) may retract with the adjacent Co^T-O species (step $\mathbf{b_1}$), giving rise to NO_3 formation in the most stable μ-η^1(O):η^1(O) Co^T−ONO_2−Co^O conformation ($\mathbf{C_1}$). The barrier of this step is small (E_a = 0.42 eV only); thus, such on-surface development of the NO_3 adspecies can be expected to occur even at ambient temperature (in accordance with the IR experiments). Final bridging NO_3 adduct $\mathbf{C_1}$ is thermodynamically much more stable than the starting ($\mathbf{A_1}$) and intermediate ($\mathbf{B_1}$) configurations (by 1.23 and 1.83 eV, respectively). Thus, once μ-η^1(O):η^1(O)-Co^T−ONO_2−Co^O is formed it might virtually block the $Co^T\cdots Co^O$ dual sites up to very high temperatures, as direct diabatic desorption is expected to occur around 500 °C (see Figure 7b_2). Actually, before the reaction temperature reaches the level of the NO_3 release, the dissociation reaction is expected to take place earlier (step $\mathbf{b_2}'$). The barrier for such dissociation is equal to 2.25 eV, whereas the direct NO_3 desorption process needs to overwhelm the adsorption energy of 2.88 eV. As a result, the one-step direct NO_3 desorption is circumvented by the more involved two-step mechanism of $NO_{3(ads)}$ dissociation into $NO_{2(ads)}$ and $O_{(ads)}$ fragments, which next desorb separately, lowering the temperature of the overall reaction to ∼400 °C in accordance with the high-temperature IR results (see Figures 7b_1 and 8a_2).

The NO_2 to NO_3 oxidation pathway over the $Co^O\cdots Co^O$ dual site is presented in the bottom panel of Figure 11 ($\mathbf{A_2} \rightarrow \mathbf{B_2} \rightarrow \mathbf{C_2}$ sequence). It begins with the same μ-η^1(N):η^1(O)-Co^O−N(O)O−Co^O adduct but involves different nearby surface oxygen species (Co^O-O instead of Co^T-O). Initial step $\mathbf{a_2}$ consists in the transformation of the bridging NO_2 complex into a monodentate η^1-O form with E_a = 0.81 eV. Then, upon the formation of another N−O bond with rather small energy barrier (step $\mathbf{b_2}$ with E_a = 0.31 eV) a bridging μ-η^1:η^1-Co^O−ONO_2−Co^O surface complex is formed, even at ambient conditions (in line with the IR observations). The resultant μ-η^1:η^1-Co^O−ONO_2−Co^O adduct is significantly less stable than that with NO_3 attached to the $Co^T\cdots Co^O$ sites, and its desorption is expected to take place around 100 °C (see Figure 7b_2), i.e., in the same temperature region in which dissociative desorption occurs (see blue solid line in Figure 7b_2) but to a much lower extent.

Finally, it is also worth mentioning that the direct one-step formation of NO_3 from the most stable NO_2 and O adspecies is energetically quite demanding over both dual $Co^T\cdots Co^O$ and $Co^O\cdots Co^O$ centers (E_a = 3.88 and 3.4 eV, respectively), due to pronounced geometrical restrictions (see Figure S7). Such a reaction needs robust reorganization of the bond lengths in the corresponding transition states (Co−O bond is nearly broken when the incipient N−O bond is just emerging). Thus, being kinetically hindered is not expected to play any significant role in the investigated reactions.

4. CONCLUSIONS

Comprehensive spin-unrestricted DFT + U/PW91 and *ab initio* thermodynamic calculations combined with IR and isotopic exchange measurements revealed large variety of N- and O-bound monodentate (η^1), bidentate (η^2), bridging bidentate (μ-η^2), and bridging monodentate (μ-η^1:η^1) adducts of the associatively adsorbed NO_2 and NO_3 on the (100) surface of cobalt spinel nanocubes. The most stable were the bridging μ-η^1(O):η^1(O)-Co^T−ONO−Co^O (−1.91 eV) and chelating η^2(O,O)-NO_2−Co^T (−1.87 eV) adducts associated with the dual $Co^T_{2c}\cdots Co^O_{5c}$ sites. The parallel μ-η^1(O):η^1(O)-Co^O−ONO−Co^O (−1.25 eV) and η^2(O,O)-NO_2−Co^O (−1.57 eV) surface complexes of $Co^O_{2c}\cdots Co^O_{5c}$ centers were more feebly bound. Analysis of the DOS structure, spin density, and the atomic partial charge repartition allowed for detailed interpretation of the electronic structure of the most stable NO_2 and NO_3 surface adducts. It was shown that the hybridization extent of the key σ and π/π^* orbitals of NO_2 and NO_3 with the relevant 3d orbitals of the Co^T and Co^O sites exhibits strongly uneven involvement of both cobalt centers in the ligation process. The constructed thermodynamic $\Theta_{NO_2} = f(p_{NO_2}, T)$ and $d\Theta_{NO_2}/dT$ vs T diagrams were successfully used for quantitative interpretation of the NO_2 and NO_3 adsorption/desorption processes on the (100) surface in wide range of temperatures and pressures. It was argued that the $Co^T\cdots Co^O$ sites being blocked act as spectators, whereas the $Co^O\cdots Co^O$ centers play the role of active centers in catalytic processes such as NO to NO_2 oxidation or $N^{16}O/N^{18}O$ isotopic exchange. The spectroscopic signatures and stability of the identified NO_x adspecies were established in variable temperature IR measurements. The diagnostic IR band for the bridging $Co^T-NO_2-Co^O$ adducts appears at 1680 cm^{-1}, for the chelating, mondentate N- and O-bound Co^T−NOO complexes at 1315, 1260, and 1525 cm^{-1}, whereas for the bridging Co^T-NO_3-CoO and the monodentate Co^T-NO_3 adducts at 1625 and 1560 cm^{-1}, respectively. A complex intermolecular surface O ↔NO ↔ NO_2↔ NO_3 dynamics was

https://dx.doi.org/10.1021/acs.jpcc.0c06195
J. Phys. Chem. C 2020, 124, 19681−19697

established and applied for elucidation the intricate mechanism of NO_2 and NO_3 desorption, NO oxidation, and isotopic exchange, providing a suitable background for other catalytic processes involving nitrogen oxides. A notable agreement between the experiment and theory substantiates the proposed identification of the most important NO_x adspecies and the developed molecular mechanism of their surface and interfacial dynamics.

■ ASSOCIATED CONTENT

Supporting Information

The Supporting Information is available free of charge at https://pubs.acs.org/doi/10.1021/acs.jpcc.0c06195.

Slab model of Co_3O_4 (100) surface; chemical potential of the gas phase molecules and Langmuir isotherm approach; spinel sample characterization; Co_3O_4 bulk modeling: experiment versus theory; electronic and magnetic structure of the cobalt spinel (100) surface; selected modes of NO adsorption on the (100) Co_3O_4 surface; surface free energy of the ON-Co^{O}_{5c} covered surface; direct NO_2 to NO_3 on-surface oxidation mechanism (PDF)

■ AUTHOR INFORMATION

Corresponding Author

Filip Zasada − *Faculty of Chemistry, Jagiellonian University, PL 30-387 Krakow, Poland;* orcid.org/0000-0003-2815-0644; Phone: +48 12 686 24 91; Email: zasada@chemia.uj.edu.pl

Authors

Pâmella Vasconcelos Borges Pinho − *Faculty of Chemistry, Jagiellonian University, PL 30-387 Krakow, Poland*

Witold Piskorz − *Faculty of Chemistry, Jagiellonian University, PL 30-387 Krakow, Poland;* orcid.org/0000-0002-3462-436X

Camillo Hudy − *Faculty of Chemistry, Jagiellonian University, PL 30-387 Krakow, Poland*

Janusz Janas − *Faculty of Chemistry, Jagiellonian University, PL 30-387 Krakow, Poland*

Joanna Gryboś − *Faculty of Chemistry, Jagiellonian University, PL 30-387 Krakow, Poland;* orcid.org/0000-0002-9777-0268

Kinga Góra-Marek − *Faculty of Chemistry, Jagiellonian University, PL 30-387 Krakow, Poland;* orcid.org/0000-0002-1296-9244

Zbigniew Sojka − *Faculty of Chemistry, Jagiellonian University, PL 30-387 Krakow, Poland*

Complete contact information is available at: https://pubs.acs.org/10.1021/acs.jpcc.0c06195

Author Contributions

The manuscript was written through contributions of all authors.

Notes

The authors declare no competing financial interest.

■ ACKNOWLEDGMENTS

This work was supported by the Polish National Science Center (NCN) Project OPUS-14, No 2017/27/B/ST4/01155. Camillo Hudy has been partly supported by the Doctoral Project POWR.03.02.00-00-I004/16. Prof. Zbigniew Sojka dedicates this paper to the memory of mgr Mieczyslaw Ciemiega, an unforgettable chemistry professor in the Tadeusz Kosciuszko High School in Lubaczow, Poland.

■ ABBREVIATIONS

(111)-S, bare stoichiometric cobalt spinel termination; (111)-V_O, termination defected by surface oxygen vacancy; Co^O, cobalt in octahedral site; Co^T, cobalt in tetrahedral site; DFT +U, density functional theory with Hubbard corrected functionals; ER, Eley−Rideal; FPT, first-principles thermodynamics; GGA, generalized gradient approximation; HL, Hinshelwood−Langmuir; MvK, Mars−van Krevelen; O_{ads}, monatomic suprafacial oxygen; O_{surf}, surface lattice oxygen; ROS, reactive oxygen species; V_O, oxygen vacancy

■ REFERENCES

(1) Boningari, T.; Smirniotis, P. G Impact of nitrogen oxides on the environment and human health: Mn-based materials for the NO_x abatement. *Curr. Opin. Chem. Eng.* **2016**, *13*, 133−141.

(2) Kašpar, J.; Fornasiero, P.; Hickey, N. Automotive catalytic converters: current status and some perspectives. *Catal. Today* **2003**, *77*, 419−449.

(3) Brown, S. S.; Ryerson, B.; Wollny, A. G.; Brock, C. A.; Peltier, R.; Sullivan, A. P.; Weber, R. J.; Dube, W. P.; Trainer, M.; Meagher, J. F.; et al. Variability in Nocturnal Nitrogen Oxide Processing and Its Role in Regional Air Quality. *Science* **2006**, *311*, 67−70.

(4) Brown, S. S.; Stutz, J. Nighttime Radical Observations and Chemistry. *Chem. Soc. Rev.* **2012**, *41*, 6405−6447.

(5) Louw, R.; van Ham, J.; Nieboer, H. Nitrogen Trioxide: Key Intermediate in the Chemistry of Polluted Air? *J. Air Pollut. Control Assoc.* **1973**, *23* (8), 716−716.

(6) Rodriguez, J. A.; Jirsak, T.; Liu, G.; Hrbek, J.; Dvorak, J.; Maiti, A. Chemistry of NO_2 on Oxide Surfaces: Formation of NO_3 on TiO_2(110) and NO_2↔O Vacancy Interactions. *J. Am. Chem. Soc.* **2001**, *123*, 9597−9605.

(7) Garin, F. Mechanism of NO_x decomposition. *Appl. Catal., A* **2001**, *222*, 183−219.

(8) Granger, P.; Parvulescu, V. I. Catalytic NO_x Abatement Systems for Mobile Sources: From Three-Way to Lean Burn after-Treatment Technologies. *Chem. Rev.* **2011**, *111*, 3155−3207.

(9) Imanaka, N.; Masui, T. Advances in Direct NO_x Decomposition Catalysts. *Appl. Catal., A* **2012**, *431*−*432*, 1−8.

(10) Kato, S.; Yoshizawa, T.; Kakuta, N.; Akiyama, S.; Ogasawara, M.; Wakabayashi, T.; Nakahara, Y.; Nakata, S. Preparation of Apatite-Type-Silicate-Supported Precious Metal Catalysts for Selective Catalytic Reduction of NO_x. *Res. Chem. Intermed.* **2008**, *34*, 703−708.

(11) Song, W.; Liu, J.; Zheng, H.; Ma, S.; Wei, Y.; Duan, A.; Jiang, G.; Zhao, Z.; Hensen, E. J. M. A Mechanistic DFT Study of Low Temperature SCR of NO with NH_3 on $MnCe_{1-x}O_2$(111). *Catal. Sci. Technol.* **2016**, *6*, 2120−2128.

(12) More, P. M.; Dongare, M. K.; Umbarkar, S. B.; Granger, P.; Dujardin, C. Bimetallic Au-Ag/Al_2O_3 as Efficient Catalysts for the Hydrocarbon Selective Reduction of NO_x From Lean Burn Engine Exhaust. *Catal. Today* **2018**, *306*, 23−31.

(13) Gao, X.; Du, X. S.; Cui, L. W.; Fu, Y. C.; Luo, Z. Y.; Cen, K. F. A Ce-Cu-Ti Oxide Catalyst for the Selective Catalytic Reduction of NO with NH_3. *Catal. Commun.* **2010**, *12*, 255−258.

(14) Lin, Q. C.; Li, J. H.; Ma, L.; Hao, J. M. Selective Catalytic Reduction of NO with NH_3 over Mn-Fe/USY Under Lean Burn Conditions. *Catal. Today* **2010**, *151*, 251−256.

(15) Cheng, J.; Han, S.; Ye, Q.; Cheng, S.; Kang, T.; Dai, H. Effects of Hydrothermal Aging at High and Low Temperatures on the Selective Catalytic Reduction of NO_x with NH_3 over Cu/SAPO-34. *Res. Chem. Intermed.* **2019**, *45*, 2023−2044.

(16) Yang, S.; Wang, Ch.; Li, J.; Yan, N.; Ma, L.; Chang, H. Low Temperature Selective Catalytic Reduction of NO with NH_3 over Mn-Fe spinel: Performance, Mechanism and Kinetic study. *Appl. Catal., B* **2011**, *110*, 71−80.

(17) Li, K.; Tang, X.; Yi, H.; Ning, P.; Song, J.; Wang, J. Mechanism of Catalytic Oxidation of NO over $MnCoCeO_x$ Catalysts with the Aid of Nonthermal Plasma at Low Temperature. *Ind. Eng. Chem. Res.* **2011**, *50*, 11023−11028.
(18) Madia, G.; Koebel, M.; Elsener, M.; Wokaun, A. Side Reactions in the Selective Catalytic Reduction of NO_x with Various NO_2 Fractions. *Ind. Eng. Chem. Res.* **2002**, *41*, 3512−3517.
(19) Epling, W. S.; Campbell, L. E.; Yezerets, A.; Currier, N. W.; Parks, J. E., II Overview of the Fundamental Reactions and Degradation Mechanisms of NO_x Storage/Reduction Catalysts. *Catal. Rev.: Sci. Eng.* **2004**, *46*, 163−245.
(20) Shojaee, K.; Haynes, B. S.; Montoya, A. Molecular Modelling of the Decomposition of NH_3 over CoO(100). *Mater. Chem. Phys.* **2015**, *156*, 141−149.
(21) Beale, A. M.; Gao, F.; Lezcano-Gonzalez, I.; Peden, C. H. F.; Szanyi, J. Recent Advances in Automotive Catalysis for NO_x Emission Control by Small-Pore Microporous Materials. *Chem. Soc. Rev.* **2015**, *44*, 7371−7405.
(22) Shojaee, K.; Haynes, B. S.; Montoya, A. The Role of Oxygen During the Catalytic Oxidation of Ammonia on Co_3O_4(100). *Appl. Surf. Sci.* **2014**, *316*, 355−365.
(23) Li, L. D.; Shen, Q.; Cheng, J.; Hao, Z. P. Catalytic Oxidation of NO over TiO_2 Supported Platinum Clusters I. Preparation, Characterization and Catalytic Properties. *Appl. Catal., B* **2010**, *93*, 259−266.
(24) Wen, Y. X.; Zhang, C. B.; He, H.; Yu, Y. B.; Teraoka, Y. Catalytic Oxidation of Nitrogen Monoxide over $La_{1-x}Ce_xCoO_3$ Perovskites. *Catal. Today* **2007**, *126*, 400−405.
(25) Yung, M. M.; Holmgreen, E. M.; Ozkan, U. S. Cobalt-based Catalysts Supported on Titania and Zirconia for the Oxidation of Nitric Oxide to Nitrogen Dioxide. *J. Catal.* **2007**, *247*, 356−367.
(26) Despres, J.; Elsener, M.; Koebel, M.; Krocher, O.; Schnyder, B.; Wokaun, A. Catalytic Oxidation of Nitrogen Monoxide over Pt/SiO_2. *Appl. Catal., B* **2004**, *50*, 73−82.
(27) Olsson, L.; Fridell, E. The Influence of Pt Oxide Formation and Pt Dispersion on the Reactions $NO_2 \Leftrightarrow NO+1/2\ O_2$ over Pt/Al_2O_3 and $Pt/BaO/Al_2O_3$. *J. Catal.* **2002**, *210*, 340−353.
(28) Xue, E.; Seshan, K.; Ross, J. R. H. Roles of Supports, Pt Loading and Pt Dispersion in the Oxidation of NO to NO_2 and of SO_2 to SO_3. *Appl. Catal., B* **1996**, *11*, 65−79.
(29) Fan, T.; Dou, L.; Zhang, H. Nonprecious Mixed Oxide Catalysts Co_3AlO_4 and Co_2NiAlO_4 Derived From Nanoflowerlike Cobalt-Based Hydrotalcites for Highly Efficient Oxidation of Nitric Oxide. *RSC Adv.* **2016**, *6*, 110274−110287.
(30) Gao, F.; Chu, Ch.; Zhu, W.; Tang, X.; Yi, H.; Zhang, R. High-efficiency catalytic oxidation of nitric oxide over spherical MnCo spinel catalyst at low temperature. *Appl. Surf. Sci.* **2019**, *479*, 548−556.
(31) Fino, D.; Russo, N.; Saracco, G.; Specchia, V. Catalytic removal of NO_x and Diesel Soot over Nanostructured Spinel-Type Oxides. *J. Catal.* **2006**, *242*, 38−47.
(32) Zhao, M.; Deng, J.; Liu, J.; Liu, J.; Li, Y.; Liu, J.; Duan, Z.; Xiong, J.; Zhao, Z.; Wei, Y.; et al. Roles of Surface-Active Oxygen Species on 3DOM Cobalt-Based Spinel Catalysts $M_xCo_{3-x}O_4$ (M = Zn and Ni) for NO_x-Assisted Soot Oxidation. *ACS Catal.* **2019**, *9*, 7548−7567.
(33) Eom, W.-H.; Ayoub, M.; Yoo, K.-S. Catalytic Decomposition of N_2O at Low Temperature by Reduced Cobalt Oxides. *J. Nanosci. Nanotechnol.* **2016**, *16*, 4647−4654.
(34) Zasada, F.; Stelmachowski, P.; Maniak, G.; Paul, J.-F.; Kotarba, A.; Sojka, Z. Potassium Promotion of Cobalt Spinel Catalyst for N_2O Decomposition — Accounted by Work Function Measurements and DFT Modelling. *Catal. Lett.* **2009**, *127*, 126−131.
(35) Yakovlev, A. L.; Zhidomirov, G. M.; Van Santen, R. N_2O Decomposition Catalysed by Transition Metal Ions. *Catal. Lett.* **2001**, *75*, 45−48.
(36) Piskorz, W.; Zasada, F.; Stelmachowski, P.; Kotarba, A.; Sojka, Z. Decomposition of N_2O over the Surface of Cobalt Spinel: A DFT Account of Reactivity Experiments. *Catal. Today* **2008**, *137*, 418−422.
(37) Kim, M.-J.; Lee, S.-J.; Ryu, I.-S.; Moon, S.-H.; Jeon, M.-W.; Ko, C. H.; Jeon, S. G. Understanding the Effect of NO Adsorption on Potassium-Promoted Co_3O_4 for N_2O Decomposition. *Catal. Lett.* **2017**, *147*, 2886−2892.
(38) Aslam, R.; Usman, M. R.; Irfan, M. F. A Comparative Study of LHHW and ER Kinetic Models for NO Oxidation over Co_3O_4 Catalyst. *J. Environ. Chem. Eng.* **2016**, *4*, 2871−2877.
(39) Shang, Z.; Sun, M.; Che, X.; Wang, W.; Wang, L.; Cao, X.; Zhan, W.; Guo, Y.; Guo, Y.; Lu, G. The Existing States of Potassium Species in K-doped Co_3O_4 Catalysts and Their Influence on the Activities for NO and Soot Oxidation. *Catal. Sci. Technol.* **2017**, *7*, 4710−4719.
(40) Akamatsu, T.; Itoh, T.; Izu, N.; Shin, W. NO and NO_2 Sensing Properties of WO_3 and Co_3O_4 Based Gas Sensors. *Sensors* **2013**, *13*, 12467−12481.
(41) Zhang, B.; Cheng, M.; Liu, G.; Gao, Y.; Zhao, L.; Li, S.; Wang, Y.; Liu, F.; Liang, X.; Zhang, T.; et al. Room Temperature NO_2 Gas Sensor Based on Porous Co_3O_4 Slices/Reduced Graphene Oxide Hybrid. *Sens. Actuators, B* **2018**, *263*, 387−399.
(42) Li, K.; Luo, Y.; Liu, B.; Gao, L.; Duan, G. High-Performance NO_2-Gas Sensing of Ultrasmall $ZnFe_2O_4$ Nanoparticles Based on Surface Charge Transfer. *J. Mater. Chem. A* **2019**, *7*, 5539−5551.
(43) Hu, L.; Peng, Q.; Li, Y. Selective Synthesis of Co_3O_4 Nanocrystal with Different Shape and Crystal Plane Effect on Catalytic Property for Methane Combustion. *J. Am. Chem. Soc.* **2008**, *130*, 16136−16137.
(44) Su, D.; Dou, S.; Wang, G. Single Crystalline Co_3O_4 Nanocrystals Exposed with Different Crystal Planes for Li-O_2 Batteries. *Sci. Rep.* **2015**, *4*, 5767−5776.
(45) Zhou, K.; Li, Y. Catalysis Based on Nanocrystals with Well-Defined Facets. *Angew. Chem., Int. Ed.* **2012**, *51*, 602−613.
(46) Zasada, F.; Janas, J.; Piskorz, W.; Gorczyńska, M.; Sojka, Z. Total Oxidation of Lean Methane over Cobalt Spinel Nanocubes Controlled by the Self-Adjusted Redox State of the Catalyst: Experimental and Theoretical Account for Interplay Between the Langmuir-Hinshelwood and Mars-Van Krevelen Mechanisms. *ACS Catal.* **2017**, *7*, 2853−2867.
(47) Zasada, F.; Piskorz, W.; Janas, J.; Gryboś, J.; Indyka, P.; Sojka, Z. Reactive Oxygen Species on the (100) Facet of Cobalt Spinel Nanocatalyst and Their Relevance in $^{16}O_2/^{18}O_2$ Isotopic Exchange, deN_2O, and deCH_4 processes - a Theoretical and Experimental Account. *ACS Catal.* **2015**, *5*, 6879−6892.
(48) Liu, X.; Qiu, G.; Li, X. Shape-controlled Synthesis and Properties of Uniform Spinel Cobalt Oxide Nanocubes. *Nanotechnology* **2005**, *16*, 3035−3040.
(49) Montoya, A.; Haynes, B. S. Periodic Density Functional study of Co_3O_4 Surfaces. *Chem. Phys. Lett.* **2011**, *502*, 63−68.
(50) Shojaee, K.; Montoya, A.; Haynes, B. S. Insight into Oxygen Stability and Vacancy Formation on Co_3O_4 Model Slabs. *Comput. Mater. Sci.* **2013**, *72*, 15−25.
(51) Perdew, J. P.; Chevary, J. A.; Vosko, S. H.; Jackson, K. A.; Pederson, M. R.; Singh, D. J.; Fiolhais, C. Atoms, Molecules, Solids, and Surfaces: Applications of the Generalized Gradient Approximation for Exchange and Correlation. *Phys. Rev. B: Condens. Matter Mater. Phys.* **1992**, *46*, 6671−6687.
(52) Zasada, F.; Piskorz, W.; Sojka, Z. Cobalt Spinel at Various Redox Conditions: DFT+U Investigations into the Structure and Surface Thermodynamics of the (100) Facet. *J. Phys. Chem. C* **2015**, *119*, 19180−19191.
(53) Selcuk, S.; Selloni, A. DFT+U Study of the Surface Structure and Stability of Co_3O_4(110): Dependence on U. *J. Phys. Chem. C* **2015**, *119*, 9973−9979.
(54) Monkhorst, H. J.; Pack, J. D. Special Points for Brillouin-Zone Integrations. *Phys. Rev. B* **1976**, *13*, 5188−5192.
(55) Methfessel, M.; Paxton, A. T. High-Precision Sampling for Brillouin-Zone Integration in Metals. *Phys. Rev. B: Condens. Matter Mater. Phys.* **1989**, *40*, 3616−3621.

https://dx.doi.org/10.1021/acs.jpcc.0c06195
J. Phys. Chem. C 2020, 124, 19681−19697

(56) Liu, X.; Prewitt, C. T. High-temperature X-ray Diffraction Study of Co_3O_4: Transition From Normal to Disordered Spinel. *Phys. Chem. Miner.* **1990**, *17*, 168−172.
(57) Bader, R. F. W. A Quantum Theory of Molecular Structure and its Applications. *Chem. Rev.* **1991**, *91*, 893−928.
(58) Henkelman, G.; Uberuaga, B. P.; Jónsson, H. Climbing Image Nudged Elastic Band Method for Finding Saddle Points and Minimum Energy Paths. *J. Chem. Phys.* **2000**, *113*, 9901−1.
(59) Reuter, K.; Scheffler, M. Composition and Structure of the RuO_2(110) Surface in an O and CO Environment: Implications for the Catalytic Formation of CO_2. *Phys. Rev. B: Condens. Matter Mater. Phys.* **2003**, *68*, 045407−045418.
(60) Sillar, K.; Hofmann, A.; Sauer, J. Ab Initio Study of Hydrogen Adsorption in MOF-5. *J. Am. Chem. Soc.* **2009**, *131*, 4143−4150.
(61) Zasada, F.; Piskorz, W.; Cristol, S.; Paul, J.-F.; Kotarba, A.; Sojka, Z. Periodic Density Functional Theory and Atomistic Thermodynamic Studies of Cobalt Spinel Nanocrystals in Wet Environment: Molecular Interpretation of Water Adsorption Equilibria. *J. Phys. Chem. C* **2010**, *114*, 22245−22253.
(62) Pinho, P. V. B.; Gryboś, J.; Hudy, C.; Janas, J.; Góra-Marek, K.; Zasada, F.; Sojka, Z. Interaction of Nitric Oxide with the (100) Surface of Cobalt Spinel Nanocubes - A Comprehensive DFT, Atomistic Thermodynamic, IR and TPD Account. *Appl. Surf. Sci.* **2020**, *513*, 145835−145845.
(63) Han, X.; Yin, X. Density Functional Theory Study of the NO_2-Sensing Mechanism on a WO_3 (001) Surface: the Role of Surface Oxygen Vacancies in the Formation of NO and NO_3. *Mol. Phys.* **2016**, *114*, 3546−3555.
(64) Broqvist, P.; Grönbeck, H.; Fridell, E.; Panas, I. NO_x Storage on BaO: Theory and Experiment. *Catal. Today* **2004**, *96*, 71−78.
(65) Jirsak, T.; Kuhn, M.; Rodriguez, J. A. Chemistry of NO_2 on Mo(110): Decomposition Reactions and Formation of MoO_2. *Surf. Sci.* **2000**, *457*, 254−266.
(66) Inger, M.; Wilk, M.; Saramok, M.; Grzybek, G.; Grodzka, A.; Stelmachowski, P.; Makowski, W.; Kotarba, A.; Sojka, Z. Cobalt Spinel Catalyst for N_2O Abatement in the Pilot Plant Operation-Long-Term Activity and Stability in Tail Gases. *Ind. Eng. Chem. Res.* **2014**, *53*, 10335−10342.
(67) Hadjiivanov, K. Identification of Neutral and Charged N_xO_y Surface Species by IR Spectroscopy. *Catal. Rev.: Sci. Eng.* **2000**, *42*, 71−144.
(68) Zasada, F.; Piskorz, W.; Janas, J.; Budiyanto, E.; Sojka, Z. Dioxygen Activation Pathways Over Cobalt Spinel Nanocubes - From Molecular Mechanism into ab initio Thermodynamics and $^{16}O_2$ /$^{18}O_2$ Exchange Microkinetics. *J. Phys. Chem. C* **2017**, *121*, 24128−24143.
(69) Piskorz, W.; Zasada, F.; Stelmachowski, P.; Diwald, O.; Kotarba, A.; Sojka, Z. Computational and Experimental Investigations into N_2O Decomposition over MgO Nanocrystals from Thorough Molecular Mechanism to ab initio Microkinetics. *J. Phys. Chem. C* **2011**, *115*, 22451−22460.

https://dx.doi.org/10.1021/acs.jpcc.0c06195
J. Phys. Chem. C 2020, 124, 19681−19697